



## ORIGINAL ARTICLE

# Removal of multiple pollutants from water using noble Ag/Au/magnetite/graphene/H<sub>2</sub>O<sub>2</sub> system under light and ultrasound irradiation



Rosari Saleh<sup>a,b,\*</sup>, Saskia Andiane Hidayat<sup>a,b</sup>, Ardiansyah Taufik<sup>c</sup>, Shu Yin<sup>d</sup>

<sup>a</sup> Departemen Fisika, Fakultas MIPA-Universitas Indonesia, 16424 Depok, Indonesia

<sup>b</sup> Integrated Laboratory of Energy and Environment, Fakultas MIPA-Universitas Indonesia, 16424 Depok, Indonesia

<sup>c</sup> New Industry Creation Hatchery Center (NICHe) Tohoku University, 6-6-10 Aoba, Aramaki-Aza, Aoa-ku, Sendai, Miyagi 980-8579, Japan

<sup>d</sup> Institute of Multidisciplinary Research for Advance Materials, Tohoku University, 2-2-1 Katahira, Aoba-ku, Sendai 980-8577, Japan

Received 3 January 2021; accepted 29 March 2022

Available online 4 April 2022

## KEYWORDS

Magnetic;  
H<sub>2</sub>O<sub>2</sub>;  
Pollutant;  
Noble metals

**Abstract** Ag/Au/Fe<sub>3</sub>O<sub>4</sub>/graphene composites prepared by a hydrothermal method demonstrated excellent activation of H<sub>2</sub>O<sub>2</sub> and were used to degrade methylene blue (MB) in solution in the presence of organic acids and inorganic ions under light and ultrasound irradiation. The physicochemical properties of the obtained composites were characterized using various methods. The results showed that the composites exhibited excellent magnetic properties, crystallinity, and stability. The results of catalysis experiments revealed that the removal efficiency of MB increased when Ag and Au were both incorporated into the Fe<sub>3</sub>O<sub>4</sub>/graphene/H<sub>2</sub>O<sub>2</sub> system compared with the removal efficiency achieved with separate Ag-Fe<sub>3</sub>O<sub>4</sub>/graphene/H<sub>2</sub>O<sub>2</sub> and Au-Fe<sub>3</sub>O<sub>4</sub>/graphene/H<sub>2</sub>O<sub>2</sub> systems, indicating a substantial synergistic interaction between the two metallic nanoparticles and the Fe<sub>3</sub>O<sub>4</sub>/graphene/H<sub>2</sub>O<sub>2</sub> systems. The presence of an organic acid accelerated degradation of the MB/H<sub>2</sub>O<sub>2</sub> system, whereas almost all of the investigated anions inhibited the degradation of MB; their inhibition effects followed the order CO<sub>3</sub><sup>2-</sup> > NO<sub>3</sub><sup>-</sup> > Cl<sup>-</sup> > F<sup>-</sup> > H<sub>2</sub>PO<sub>4</sub><sup>-</sup> > SO<sub>4</sub><sup>2-</sup> > I<sup>-</sup>. Cations of Na<sup>+</sup>, K<sup>+</sup>, Ca<sup>2+</sup>, and Mg<sup>2+</sup> also suppressed MB degradation, likely because of the influence of Cl<sup>-</sup> coexisting in the solutions.

© 2022 The Author(s). Published by Elsevier B.V. on behalf of King Saud University. This is an open access article under the CC BY-NC-ND license (<http://creativecommons.org/licenses/by-nc-nd/4.0/>).

\* Corresponding author at: Departemen Fisika, Fakultas MIPA-Universitas Indonesia, 16424 Depok, Indonesia.

E-mail address: [rosari.saleh@ui.ac.id](mailto:rosari.saleh@ui.ac.id) (R. Saleh).

Peer review under responsibility of King Saud University.



## 1. Introduction

In recent years, photocatalysis reactions using iron oxide as the photocatalyst have received considerable attention for water treatment (Mishra and Chun, 2015). Among various iron oxides, Fe<sub>3</sub>O<sub>4</sub> nanoparticles (NPs) are an essential catalyst for this purpose because of their good catalytic and adsorptive properties and high biocompatibility

(Xuan et al., 2011). Moreover, Fe<sub>3</sub>O<sub>4</sub> NPs are ferromagnetic, which enables easy and rapid separation of the catalyst from solutions (Ahmad et al., 2017; Yaqoob et al., 2020a; Zhu et al., 2020). However, the small size of Fe<sub>3</sub>O<sub>4</sub> NPs can lead to agglomeration and floating during water treatment. In order to overcome these impediments, numerous strategies have been utilized. These efforts include the addition of some 2D materials into the Fe<sub>3</sub>O<sub>4</sub> NPs such as graphene (Vinothkannan et al., 2015), CNTs (Yang et al., 2016), and MoS<sub>2</sub> (Wang et al., 2021).

Graphene, a two-dimensional sheet of *sp*<sup>2</sup>-hybridized carbon, is considered as a new class of graphitic material and has been explored for the removal of water contaminants because of its high specific surface area, optical transparency, and special electronic transport properties (Perreault et al., 2015). The integration of graphene with NPs to form a composite NP/graphene catalyst result in a material with special features and can hinder agglomeration (Padhi et al., 2017; Singh et al., 2017; Yaqoob et al., 2020b). Moreover, the catalytic activity and durability can be improved because graphene favors better dispersion of NPs (Gu and Zhu, 2020). Therefore, the integration Fe<sub>3</sub>O<sub>4</sub> NPs with graphene, resulting in an improved magnetic material for pollutant management (Mahalingam and Ahn, 2018).

Recently, it is reported that noble-metal such as Ag or Au has electron-storage property facilitating charge separation and can effectively hinder the recombination of electron-hole pairs and improve the efficiency of photocatalytic reaction under UV and visible light (Amoli-Diva et al., 2019; Yaqoob et al., 2020c; Yaqoob et al., n.d.; Zhang et al., 2016). The synergistic effect among Fe<sub>3</sub>O<sub>4</sub> NPs, graphene and Ag or Au will enhance the light absorption of noble-metal Fe<sub>3</sub>O<sub>4</sub> NPs and graphene composites, resulting in highly active photocatalysts (Wang et al., 2012).

Advanced oxidation processes (AOPs), which implies the generation and subsequent reaction of hydroxyl radicals ( $\cdot\text{OH}$ ), the most powerful oxidizing species, have also been successfully applied in a Fenton reaction (Fe<sup>2+</sup>/H<sub>2</sub>O<sub>2</sub>) system for the oxidation of organic pollutants (Liu et al., 2016; Nguyen et al., 2017).  $\cdot\text{OH}$  are highly reactive and effectively destroy pollutants. However, the Fe<sup>2+</sup>/H<sub>2</sub>O<sub>2</sub> system is limited by a low generation rate constant of Fe<sup>2+</sup> ions from Fe<sup>3+</sup> ions by reduction of H<sub>2</sub>O<sub>2</sub> (Barrera-Salgado et al., 2016). Therefore, irradiation with UV light (Fe<sup>2+</sup>/UV/H<sub>2</sub>O<sub>2</sub> system) can substantially accelerate the reduction of Fe<sup>3+</sup> to Fe<sup>2+</sup> ions in the presence of H<sub>2</sub>O<sub>2</sub> and lead to greater production of  $\cdot\text{OH}$ , thereby resulting in improved removal of organic dyes and pigments in solutions (Macías-Sánchez et al., 2011; Melgoza et al., 2009). Some researchers have studied ultraviolet (UV) and ultrasound (US) irradiation in conjunction with H<sub>2</sub>O<sub>2</sub> for wastewater treatment (Dükkançi, 2018; Shokri, 2018). US irradiation has been reported to disperse nanocomposites as catalysts in aqueous solutions and to clean the catalyst surface (Yehia et al., 2015). Moreover, US irradiation in aqueous solutions can accelerate chemical reactions by inducing cavitation. The collapse of microbubbles can potentially create microscopic turbulence and extreme localized temperatures and pressures, leading to the pyrolysis of water molecules and the generation of  $\cdot\text{OH}$  (Wang et al., 2005). In addition, sonication can induce acoustic streaming, which can convert sound into kinetic energy, representing a powerful tool to intensify mass transfer (Kumar et al., 2006; von Piechowski et al., 1992). We speculated that a synergistic effect between sonochemistry and photocatalysis could enhance the degradation rate of organic pollutants.

In addition to dye-containing industrial effluents in industrial wastewater, numerous inorganic contaminants are also present (Ahmad et al., 2015; Luciano et al., 2020). Dissolved organic matter, such as low-molecular-weight natural organic acids (LMOAs) produced by decomposition of animal and plant residues, is abundant in the aquatic environment (Brinkmann et al., 2003). These LMOAs can influence the degradation of organic pollutants. In addition, for color stabilization, industrial dyes contain inorganic ions such as Cl<sup>-</sup>, SO<sub>4</sub><sup>2-</sup>, NO<sub>3</sub><sup>-</sup>, H<sub>2</sub>PO<sub>4</sub><sup>-</sup>, CO<sub>3</sub><sup>2-</sup>, K<sup>+</sup>, Ca<sup>2+</sup>, and Mg<sup>2+</sup> (Czibulya et al., 2015). The presence of these inorganic contaminants can

increase the pollution load and affect the AOP mechanism. Therefore, understanding the effect of the presence of LMOAs and inorganic ions on the degradation of organic pollutants should be improved.

Studies of magnetic plasmonic catalysts toward the degradation of multiple pollutants under light and ultrasound (US) irradiation have rarely been published in the literature. In the present study, we propose a novel approach for the fabrication of a composite catalyst containing Ag and Au NPs which deposited on the surface of Fe<sub>3</sub>O<sub>4</sub> NPs on graphene (Ag/Au/Fe<sub>3</sub>O<sub>4</sub>/graphene) and investigated the photocatalytic and sonophotocatalytic behavior toward the degradation of methylene blue (MB) in the presence of (i) H<sub>2</sub>O<sub>2</sub> oxidant; (ii) a multicomponent system of H<sub>2</sub>O<sub>2</sub> and various LMOAs such as tartaric acid (TA), maleic acid (MA), formic acid (FA), oxalic acid (OA), gallic acid (GA), citric acid (CA), and ascorbic acid (AA); (iii) a multicomponent system of H<sub>2</sub>O<sub>2</sub> and various inorganic ions such as Cl<sup>-</sup>, SO<sub>4</sub><sup>2-</sup>, NO<sub>3</sub><sup>-</sup>, H<sub>2</sub>PO<sub>4</sub><sup>-</sup>, CO<sub>3</sub><sup>2-</sup>, K<sup>+</sup>, Ca<sup>2+</sup>, and Mg<sup>2+</sup>; and (iv) a multicomponent system of H<sub>2</sub>O<sub>2</sub> and a mixed solution of LMOAs and inorganic ions.

## 2. Experimental

### 2.1. Reagents and materials

Iron(II) sulfate heptahydrate (Fe(SO<sub>4</sub>)<sub>4</sub>·7H<sub>2</sub>O), silver nitrate (AgNO<sub>3</sub>), sodium hydroxide (NaOH), hydrochloroauric acid (HAuCl<sub>4</sub>), acetic acid (CH<sub>3</sub>COOH), MB, H<sub>2</sub>O<sub>2</sub>, benzoquinone (BQ), *tert*-butyl alcohol (TBA), ammonium oxalate (AO), sodium sulfate (SS), TA, MA, FA, OA, GA, CA, and AA, nickel(II) nitrate hexahydrate (Ni(NO<sub>3</sub>)<sub>2</sub>·6H<sub>2</sub>O), sodium carbonate (Na<sub>2</sub>CO<sub>3</sub>), sodium dihydrogen phosphate (NaH<sub>2</sub>PO<sub>4</sub>), sodium chloride (NaCl), sodium iodide (NaI), sodium fluoride (NaF), potassium chloride (KCl), calcium chloride dihydrate (CaCl<sub>2</sub>·2H<sub>2</sub>O), and magnesium chloride hexahydrate (MgCl<sub>2</sub>·6H<sub>2</sub>O). All chemical substances were purchased from Merck and were used without further purification. Graphene was purchased from Angstrom Materials.

### 2.2. Catalyst preparation

Fe<sub>3</sub>O<sub>4</sub> nanoparticles (NPs), Fe<sub>3</sub>O<sub>4</sub>/graphene, Ag/Fe<sub>3</sub>O<sub>4</sub>/graphene, and Au/Fe<sub>3</sub>O<sub>4</sub>/graphene composites were prepared according to the methods described in our previous studies (Saleh and Taufik, 2019a, 2019b; Taufik and Saleh, 2017a). In the present study, we used Fe<sub>3</sub>O<sub>4</sub>/graphene composites with a graphene content of 10 wt% and Ag or Au content of 25 wt%. Hereafter, the Fe<sub>3</sub>O<sub>4</sub> NPs, Fe<sub>3</sub>O<sub>4</sub>/graphene Ag/Fe<sub>3</sub>O<sub>4</sub>/graphene, and Au/Fe<sub>3</sub>O<sub>4</sub>/graphene composites are denoted as F, F-10G, Ag/F-10G, and Au/F-10G, respectively. The Ag/Au/Fe<sub>3</sub>O<sub>4</sub>/graphene (Ag/Au/F-10G) composites were synthesized using a hydrothermal method. First, HAuCl<sub>4</sub> and Ag powder were dissolved in 50 mL water and the solution was heated to boiling at 100 °C. Sodium citrate was then added to the solution, and the solution was maintained at 100 °C until its color changed to purple. Graphene and Fe<sub>3</sub>O<sub>4</sub> were added, and the resultant mixture was stirred for 30 min. After a homogeneous dark suspension was achieved, the solution was transferred to a Teflon stainless autoclave and heated at 120 °C for 12 h. The solution was then cooled to room temperature and the samples were collected by centrifugation. The final product was obtained after a drying treatment at 120 °C for 5 h.

### 2.3. Light- and ultrasound-assisted oxidation

To evaluate catalytic activities, the degradation of MB in the presence of Ag/Au-Fe<sub>3</sub>O<sub>4</sub>/graphene composites was carried out under simultaneous light and US irradiation. For comparison, the catalytic activities of the Fe<sub>3</sub>O<sub>4</sub> NPs, Fe<sub>3</sub>O<sub>4</sub>/graphene, Ag/Fe<sub>3</sub>O<sub>4</sub>/graphene, and Au/Fe<sub>3</sub>O<sub>4</sub>/graphene composites were also measured. The catalytic performance was tested under simultaneous UV/visible light and US irradiation in the presence of one of the Ag/Au/F-10G composites as illustrated in Scheme 1. In a typical experiment, an MB solution was prepared in a 100 mL glass beaker at a concentration of 20 mg/L. Then, 0.04 g of one of the Ag/Au/F-10G composites was immersed in the MB solution and stirred in the dark for 30 min to obtain a colloidal suspension. The entire assembly was placed in a cylindrical vessel sealed with Al foil to prevent other light from passing into it. The solution in the glass vessel was then exposed to US and UV/visible sources (US + UV/Vis) and the analysis process was carried out after light and/or US was applied. Under ambient conditions and stirring, the contents of the glass vessel were alternately exposed to US + UV/Vis irradiation at regular intervals for 2 h. Next, the reaction was initiated by the addition of a certain amount of H<sub>2</sub>O<sub>2</sub> solution while simultaneously irradiating the solution with US + UV/Vis. This time was considered time zero for degradation. Samples of the solution were collected every 15 min for 2 h, and after centrifugation process the extent of degradation of the solution was monitored by UV-Vis spectrophotometry (Hitachi UH5300) in the wavelength range 450–750 nm. The experiments with the addition of organic acids were conducted by adding various acids to the MB solution under otherwise identical conditions. Moreover, the influence of seven different inorganic anions (I<sup>-</sup>, F<sup>-</sup>, CO<sub>3</sub><sup>2-</sup>, SO<sub>4</sub><sup>2-</sup>, NO<sub>3</sub><sup>-</sup>, H<sub>2</sub>PO<sub>4</sub><sup>-</sup>, and Cl<sup>-</sup>) was tested using NaI, NaF, Na<sub>2</sub>CO<sub>3</sub>, SS, Ni(NO<sub>3</sub>)<sub>2</sub>·6H<sub>2</sub>O, NaH<sub>2</sub>PO<sub>4</sub>, and NaCl, respectively.

### 2.4. Characterization

The crystalline structures of all of the catalysts were studied using a Rigaku MiniFlex 600 X-ray diffractometer equipped with a Cu K $\alpha$  radiation source ( $\lambda = 1.5406 \text{ \AA}$ ); the  $2\theta$  scanning range was 10–90°. The morphologies of the samples were characterized by transmission electron microscopy (TEM) on an instrument (FEI Tecnai G2 Super Twin) equipped with an energy-dispersive X-ray (EDX) spectroscopy apparatus. For the determination of the Brunauer–Emmett–Teller (BET) surface area and pore size distribution, N<sub>2</sub> adsorption–desorption

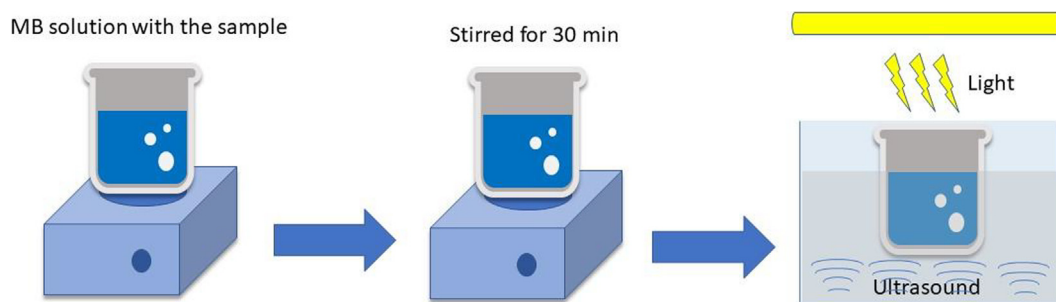
isotherms were obtained using a Quantachrome Nova 2000 system. X-ray photoelectron spectroscopy (XPS) profiles were recorded on a Physical Electronics PHI-5400 spectrometer equipped with an Al-K $\alpha$  (1486.6 eV) X-ray source. Raman spectra were recorded on a Raman microscope (Thermo Scientific DXR *xi* Raman imaging microscope) equipped with a 5 mW, 532 nm laser as a monochromatic radiation source. Magnetic measurements were carried out using a vibrating sample magnetometer (VSM, Oxford type 1.2 T). Thermogravimetric analysis (TGA) of the adsorbents was conducted using a Rigaku TG8121 thermogravimetric analyzer.

## 3. Results and discussion

### 3.1. Influence of H<sub>2</sub>O<sub>2</sub> addition on catalytic performance

An oxidant such as H<sub>2</sub>O<sub>2</sub> can inhibit charge-carrier recombination and enhance the photocatalytic oxidation of an organic substrate on a catalyst's surface (Kumar and Rao, 2015). Therefore, in the present study, the capability of H<sub>2</sub>O<sub>2</sub> as an oxidant was explored and the influence of several reaction parameters was evaluated. Prior further investigations, the blank test experiment was conducted. The effect of H<sub>2</sub>O<sub>2</sub>, visible light, UV-Light, H<sub>2</sub>O<sub>2</sub> + UV, H<sub>2</sub>O<sub>2</sub> + Vis without catalyst were investigated and the result were plotted in Fig. S1. The degradation ability of the blank test experiments is not that significant, therefore, the introducing of the catalyst is necessary to be conducted. Before studying the effect of light and ultrasound irradiation, we determined the optimum photocatalytic conditions. A series of experiments were performed to deduce the optimum conditions for removing organic dyes from solutions, including the optimum pH, catalyst dosage, and H<sub>2</sub>O<sub>2</sub> concentration. The optimum conditions for removing MB were investigated by measuring the removal of MB in an aqueous solution room temperature in the presence of composites in the dark within 2 h. The influence of pH on the removal of MB is shown in Fig. 1a. For comparison, the results for F, F-10G, Ag/F-10G, and Au/F-10G are included in the plot. Overall, the removal of MB increased as the pH was increased from 3 to 5 and decreased as the pH was further increased to 11. Notably, 57.11% removal of MB was achieved when Ag/Au/F-10G was present in the solution, whereas the MB removal by the Ag/F-10G and Au/F-10G composites was 51.39% and 48.71%, respectively.

The concentration of H<sub>2</sub>O<sub>2</sub> is known to influence the formation of active radicals for the removal of MB. Herein, the effect of the concentration of H<sub>2</sub>O<sub>2</sub> on the degradation of



Scheme 1 Sonophotocatalytic reaction illustration.

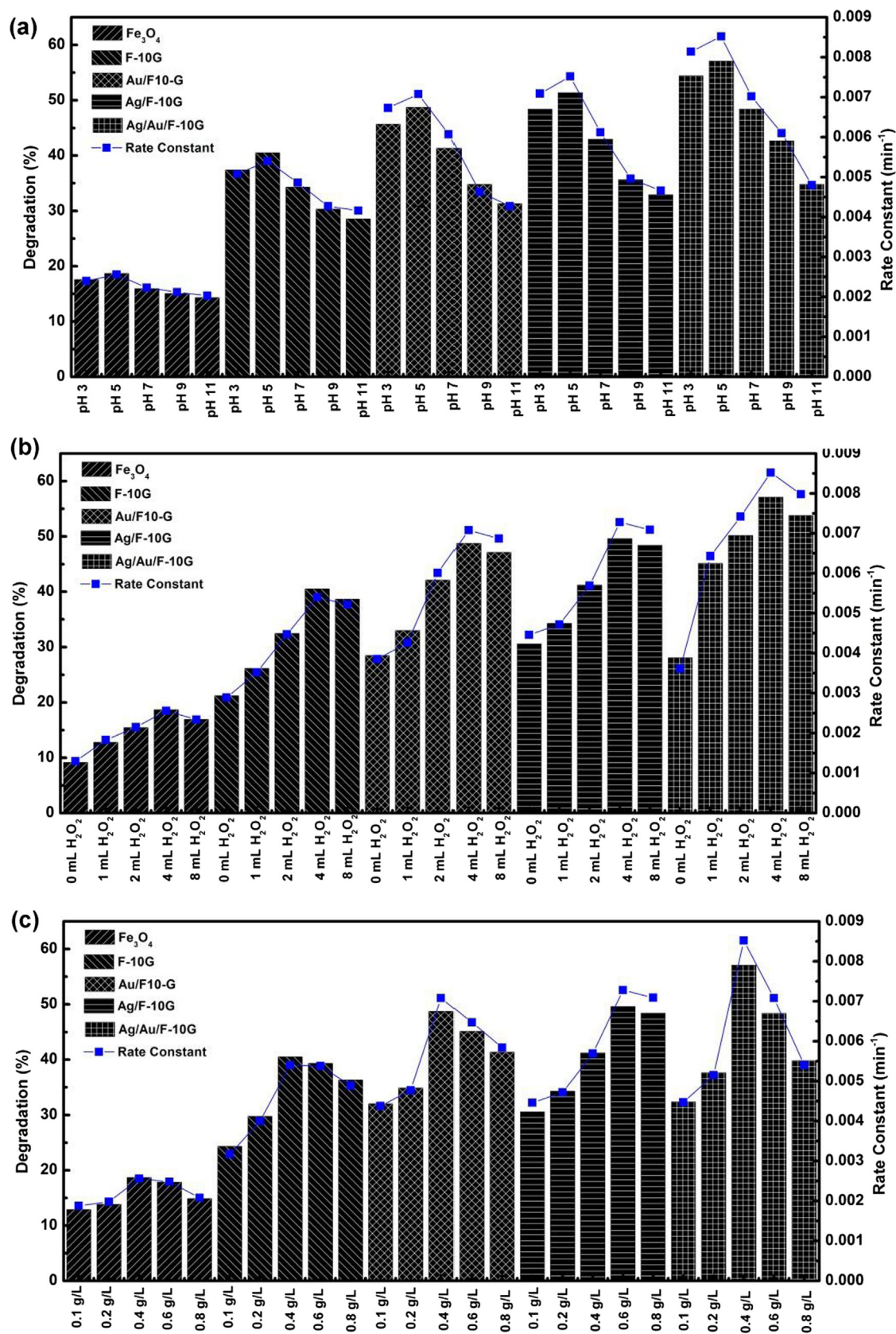


**Fig. 1** Influence of (a) pH, (b)  $\text{H}_2\text{O}_2$  concentration, and (c) catalyst dosage on the Fenton reactions of the F, F-10G, Ag/F-10G, Au/F-10G, and Ag/Au/F-10G catalyst systems under  $\text{H}_2\text{O}_2$ , UV, Vis,  $\text{H}_2\text{O}_2$  + UV, and  $\text{H}_2\text{O}_2$  + Vis reaction conditions.

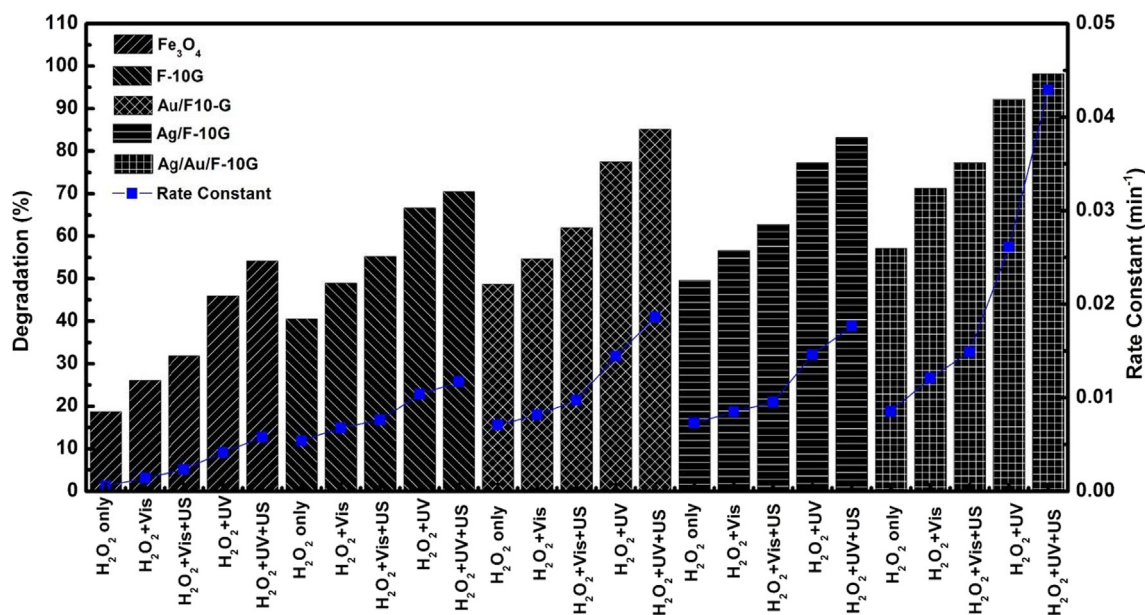


**Fig. 2** Influence of the radiation source on the Fenton reactions of the F, F-10G, Ag/F-10G, Au/F-10G, and Ag/Au/F-10G catalyst systems under H<sub>2</sub>O<sub>2</sub>, UV, Vis, H<sub>2</sub>O<sub>2</sub> + UV, and H<sub>2</sub>O<sub>2</sub> + Vis reaction conditions, and (b) reusability of the F, F-10G, Ag/F-10G, Au/F-10G, and Ag/Au/F-10G catalyst systems under H<sub>2</sub>O<sub>2</sub>, UV, Vis, H<sub>2</sub>O<sub>2</sub> + UV, and H<sub>2</sub>O<sub>2</sub> + Vis reaction conditions.

MB was evaluated. The experiment was performed in the presence of 0.4 g/L of nanocomposite in 20 mg/L MB, and the solution was kept at a constant pH of 5. Fig. 1b illustrates the effect of increasing the H<sub>2</sub>O<sub>2</sub> concentration on the removal of MB in the presence of the F, F-10G, Ag/F-10G, and Au/F-10G composite catalysts. The experimental results indicate that the degradation efficiency of MB was enhanced as the amount of H<sub>2</sub>O<sub>2</sub> was increased from 1 to 4 mL; however, the effect exhibited the opposite trend as the amount of H<sub>2</sub>O<sub>2</sub> was further increased to 8 mL. As previously mentioned, H<sub>2</sub>O<sub>2</sub> is a dominant source of reactive  $\cdot\text{OH}$  radicals (Kumar and Rao, 2015). Therefore, the concentration of H<sub>2</sub>O<sub>2</sub> is considered a critical parameter in the photocatalytic process. However, the presence of excess of H<sub>2</sub>O<sub>2</sub> can result in scavenging of  $\cdot\text{OH}$  radicals and in diminished dye degradation because the formation of radicals needed for the oxidation process is quenched (Kumar and Rao, 2015).

The effect of catalyst dosage on the removal of MB was also evaluated in solutions containing 0.1–1.0 g/L nanocomposites at the optimum pH of 5 and optimum H<sub>2</sub>O<sub>2</sub> amount of 4 mL, with a reaction time of 2 h. As depicted in Fig. 1c, an increase in catalyst dosage from 0.1 to 0.4 g/L caused a substantial enhancement in MB removal for all the composites. However, a further increase in the dosage resulted in diminished removal of MB. The optimum dosage was achieved at 0.4 g/L for all of the composites. This result can be explained by an increase in the number of reactive sites available on the catalyst surfaces. It can also be explained by an increase in the surface area provided by the higher catalyst dosage, which in turn increases the reaction contact between the organic dye and reactive species produced on the surface of the catalyst, resulting in enhancement of the degradation efficiency. Increasing the catalyst dosage, on the contrary, did not improve the MB removal but slightly lowered the degradation efficiency. This result is attributable to agglomeration of the

catalyst limiting the formation of the active radicals and inhibiting the formation of Fe<sup>2+</sup> ions, which are important in the process. On the basis of the aforementioned results, the optimized pH, H<sub>2</sub>O<sub>2</sub> amount, and catalyst dosage of 5, 4 mL, and 0.4 g/L, respectively, were used in subsequent experiments.

To evaluate the influence of the radiation source on the catalytic activity, the degradation of MB in the presence of the composites was carried out under the optimized conditions in the dark, under light irradiation, under US irradiation, and under combined light and US irradiation. The results are shown in Fig. 2. In the dark process with H<sub>2</sub>O<sub>2</sub> added, the removal of MB was 18.71%, 40.55%, 49.61%, 48.72%, and 57.11% under the optimal conditions in the presence of the F, F-10G, Ag/F-10G, Au/F-10G, and Ag/Au/F-10G catalysts, respectively. However, all of the composites exhibited remarkable performance under both UV-light irradiation alone and under simultaneous UV and US irradiation: 20 mg/L of MB was removed under UV irradiation, and complete removal of MB was achieved under simultaneous UV and US irradiation. As shown in Fig. 2, with regard to the removal of MB with the addition of H<sub>2</sub>O<sub>2</sub>, the degradation efficiency follows the order H<sub>2</sub>O<sub>2</sub> + UV + US > H<sub>2</sub>O<sub>2</sub> + UV > H<sub>2</sub>O<sub>2</sub> + Vis + US > H<sub>2</sub>O<sub>2</sub> + Vis > H<sub>2</sub>O<sub>2</sub>. Irradiation with UV light clearly leads to better degradation efficiency of MB, likely because of a synergetic effect between the photocatalytic activity of the catalyst and the reaction involving H<sub>2</sub>O<sub>2</sub> (López-Vinent et al., 2019). The conversion of H<sub>2</sub>O<sub>2</sub> to  $\cdot\text{OH}$  radicals in the presence of composites under light irradiation dramatically enhanced the oxidation process (Cuerda-Correa et al., 2020). As reported by several authors (Costa et al., 2006; Qian et al., 2018; Wan and Wang, 2017), an Fe<sup>3+</sup> ion at an interface can react with H<sub>2</sub>O<sub>2</sub> to form  $\cdot\text{OH}$  radicals through a catalytic reaction that converts Fe<sup>3+</sup> ions to Fe<sup>2+</sup> ions and  $\cdot\text{OOH}$  radicals. These  $\cdot\text{OOH}$  radicals can fur-

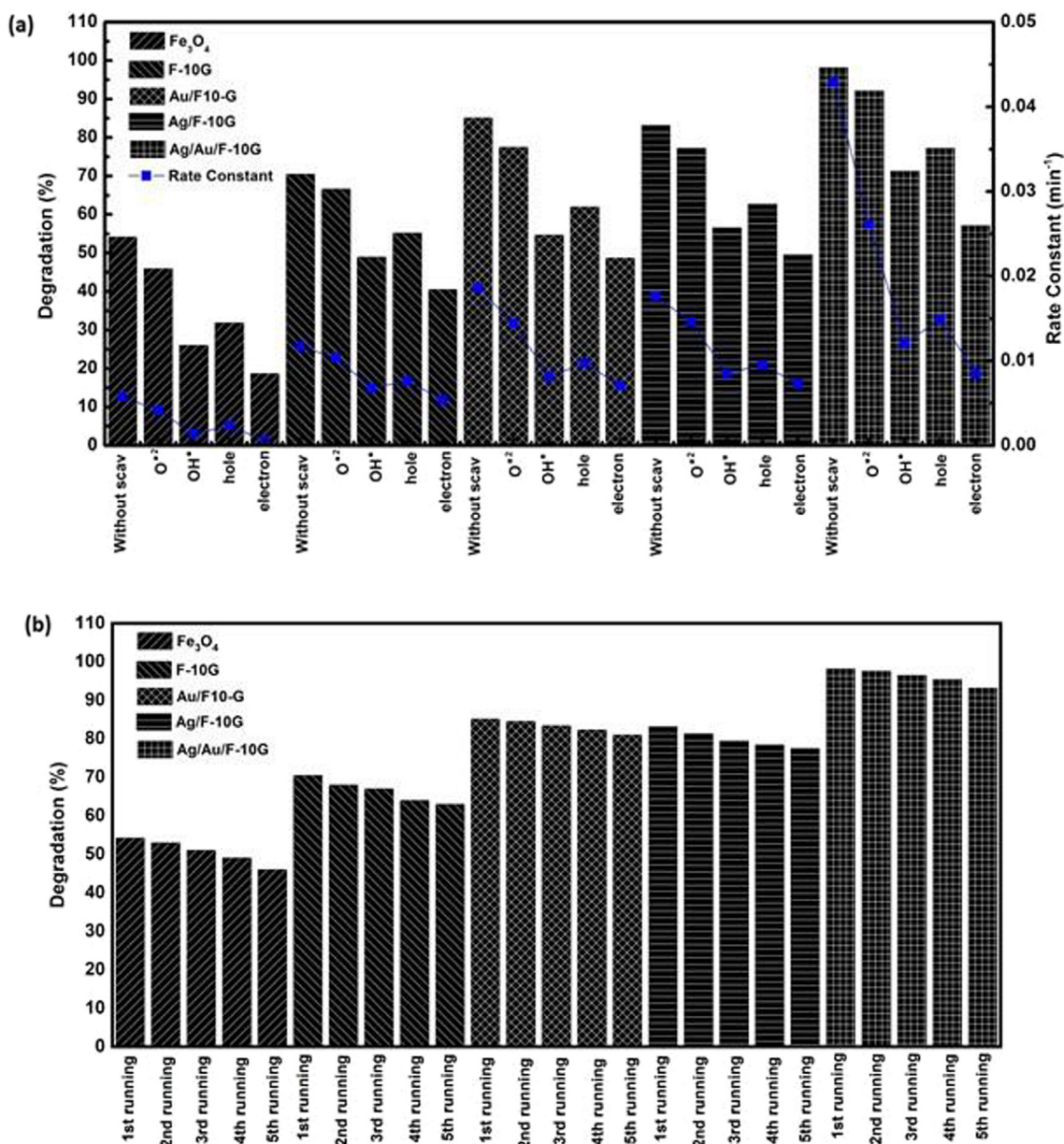


**Fig. 3** (a) Influence of the scavenger on the Fenton reactions of the F, F-10G, Ag/F-10G, Au/F-10G, and Ag/Au/F-10G catalyst systems under H<sub>2</sub>O<sub>2</sub> + MB + US + UV (b) reusability of the F, F-10G, Ag/F-10G, Au/F-10G, and Ag/Au/F-10G catalyst systems under H<sub>2</sub>O<sub>2</sub> + MB + US + UV.

ther react with Fe<sup>3+</sup> ions to create additional Fe<sup>2+</sup> ions, and the Fe<sup>2+</sup> ions can subsequently react with H<sub>2</sub>O<sub>2</sub> to produce ·OH radicals. Under light irradiation, photogenerated electrons and holes are formed. These electrons and holes interact with H<sub>2</sub>O<sub>2</sub> to produce ·OH radicals. Moreover, when light and US were used simultaneously, the cavitation in the catalytic system was enhanced, resulting in an increase of the surface area and, consequently, increased formation of ·OH radicals.

In the light + US process, ·OH radicals were produced through three mechanisms simultaneously: US + H<sub>2</sub>O<sub>2</sub>, US + H<sub>2</sub>O<sub>2</sub> + composite catalyst, and light (UV/Vis) + H<sub>2</sub>O<sub>2</sub> + composite catalyst mechanisms. (Joseph et al., 2009; López-Vinent et al., 2019) In addition, the degradation efficiency increased in the order F < F-10G < Au/F-10G < Ag/

F-10G < Ag/Au/F-10G. The Ag/Au/F-10G catalyst exhibited the best catalytic performance in the process in the presence of H<sub>2</sub>O<sub>2</sub>. The degradation rate constants ( $k_{app}$ s) were determined under the assumption that all degradation processes follow a pseudo-first-order reaction kinetic model; the values of  $k_{app}$  are shown in Fig. 2. The results indicate that, compared with UV or US irradiation alone, UV + US irradiation affords greater catalytic activities for the removal of MB in solution.

We evaluated the contribution of each species in the Ag/Au/F-10G catalyst in the photosono-Fenton reaction (H<sub>2</sub>O<sub>2</sub> + MB + US + UV) by adding specific scavengers to the solution: BQ for ·O<sub>2</sub><sup>-</sup>, TBA for ·OH, (AO) for holes, and SS for electrons (Acharya et al., 2017; von Piechowski et al., 1992). As shown in Fig. 3a, with the addition of BQ

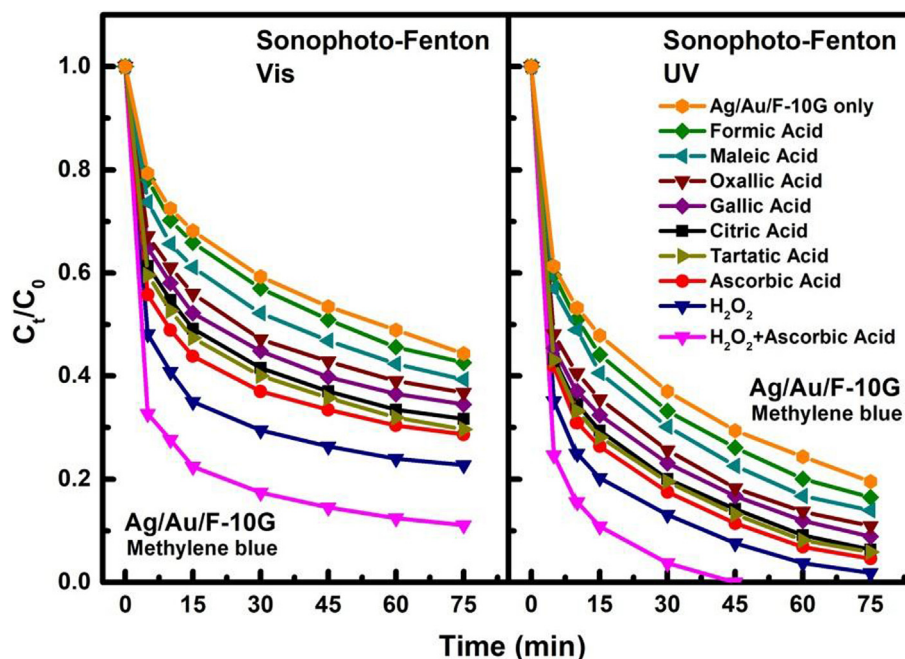


**Fig. 4** Influence of a coexisting organic acid on the Fenton reactions of Ag/Au/F-10G composites under H<sub>2</sub>O<sub>2</sub> + MB + US irradiated with visible (left) and UV (right) light.

**Table 1** Rate constant of the photo-sono-Fenton reactions of Ag/Au/F-10G in the presence of an organic acid.

Sample	Rate Constant (min <sup>-1</sup> )	
	US + Vis	US + UV
Ag/Au/F-10G only	0.0093	0.0186
FA	0.010	0.021
MA	0.011	0.023
OA	0.008	0.023
GA	0.011	0.027
CA	0.012	0.031
TA	0.013	0.032
AA	0.013	0.035
H <sub>2</sub> O <sub>2</sub>	0.015	0.045
H <sub>2</sub> O <sub>2</sub> + AA	0.022	0.099
Ag/Au/F-10G only	0.015	0.045
I <sup>-</sup>	0.015	0.040
SO <sub>4</sub> <sup>2-</sup>	0.014	0.031
H <sub>2</sub> PO <sub>4</sub> <sup>-</sup>	0.013	0.030
F <sup>-</sup>	0.013	0.028
Cl <sup>-</sup>	0.012	0.024
NO <sub>3</sub> <sup>-</sup>	0.011	0.020
CO <sub>3</sub> <sup>2-</sup>	0.011	0.019

(·O<sub>2</sub><sup>-</sup>) and AO (holes), the removal efficiency slightly decreased for all of the catalysts, suggesting that ·O<sub>2</sub><sup>-</sup> and holes are possibly active reaction intermediates. The addition of TBA to the reaction solution quenched the dye removal efficiency even further. A substantial reduction in removal efficiency was observed when SS was added to the solutions. The removal efficiency decreased from 54.18%, 70.46%, 85.13%, 83.21%, and 98.18% in the absence of a scavenger to 18.71%,

40.55%, 48.72%, 49.61%, and 57.11% for F, F-10G, Au/F-10G, Ag/F-10G, and Ag/Au/F-10G, respectively, when SS was introduced into the solution. These results suggest that electrons are important active species for the removal of MB in the sonophotocatalytic reaction. On the basis of the aforementioned results, in subsequent studies, the Ag/Au/F-10G composite was used as the catalyst, US and light irradiation were used simultaneously for irradiation, and the pH, amount of H<sub>2</sub>O<sub>2</sub>, and catalyst dosage were 5, 4 mL, and 0.4 g/L, respectively.

The reusability of all prepared samples and all degradation systems were plotted in Fig. 3b. The results indicate slight decrease of the degradation ability after several repetition degradation process. This behavior was probably due to some iron species leached in the solution or sample loss during the recovery process. However, the decrease of the degradation ability is not significant, therefore, it can be said that the samples are stable after 5th time reuse.

### 3.2. Influence of coexisting organic acid on catalytic performance of Ag/Au/F-10G

Organic acids are ubiquitous water-soluble compounds that have been detected in abundance in aquatic environments. Organic acids exhibit strong chelating ability and can strongly influence the solubility and mobility of organic compounds (Jia et al., 2015). Therefore, in the present study, the effect of the presence of acids on the degradation of MB in the presence of Ag/Au/F-10G without the addition of H<sub>2</sub>O<sub>2</sub> was first evaluated. The results (Fig. 4) show that organic acids could enhance the removal of MB in the solutions. In the absence of an organic acid, the removal efficiency of MB was only 55.64%. After 2 h of reaction, the removal efficiency followed the order of FA < MA < OA < GA < CA < TA < AA and

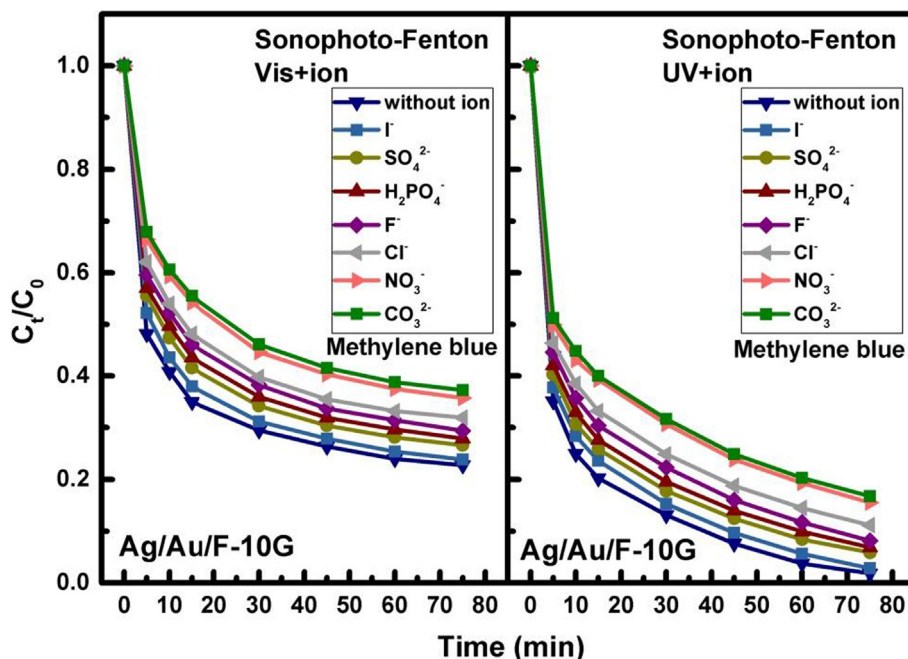


**Fig. 5** Influence of coexisting inorganic anions on the Fenton reactions of Ag/Au/F-10G composites under  $\text{H}_2\text{O}_2 + \text{MB} + \text{US}$  irradiated with visible (left) and UV (right) light.

the corresponding removal efficiency values were 57.42%, 60.7%, 63.24%, 65.51%, 68.3%, 70.33%, and 71.34% under US + visible-light irradiation, respectively. Notably, the removal of MB under US + UV-light irradiation was higher than that under US + visible-light irradiation. The experimental data in Fig. 4 were fitted using the pseudo-first-order kinetic model; the results are tabulated in Table 1. The apparent rate constant of the sonophotocatalysis process in the presence of an organic acid was higher than that of the sonophotocatalysis process in the absence of an organic acid. These results indicate that the organic acid promotes the sonophotocatalytic degradation of MB in a collaborative process. However, compared with the removal efficiency of MB in the presence of only  $\text{H}_2\text{O}_2$ , the maximum removal values of MB in the presence of only AA were still lower. Other authors have reported that an organic acid stabilizes  $\text{H}_2\text{O}_2$  in the photocatalytic reaction and that the combination of organic acid and  $\text{H}_2\text{O}_2$  exhibits high activity, enhancing the photocatalytic performance. We likewise observed that the combination of AA and  $\text{H}_2\text{O}_2$  resulted in greater removal of MB. The removal efficiency increased from 71.34% in the presence of AA alone to 88.91% when both AA and  $\text{H}_2\text{O}_2$  were present in the solutions (Fig. 4). Correspondingly, the rate constant increased from 0.0127 to  $0.0216 \text{ min}^{-1}$ .

According to the literature (Sun et al., 2009, 2017), an  $\alpha$ -OH, hydroxyl group, or carboxylic group in the chemical structure of an organic acid can influence the photocatalytic degradation efficiency. The photocatalytic degradation of organic dyes has been reported to be strongly affected by the number of carboxylic groups (Jia et al., 2015) and/or  $\alpha$ -OH groups (Sun et al., 2017) in the reaction solution. In the present study, the degradation efficiency of the photocatalyst in the presence of an organic acid was found to follow the order AA (vinylogous carboxylic groups) > TA (two  $\alpha$ -OH groups and two carboxylic groups) > CA (one  $\alpha$ -OH group and three

carboxylic groups) > GA (three hydroxyl groups and one carboxylic groups) > OA (two carboxylic groups) > MA (two carboxylic groups) > FA (one carboxylic group). These results indicate that the degradation efficiency was not strongly influenced by the number of  $\alpha$ -OH groups and exhibited no linear correlation with the number of carboxylic groups. However, the removal efficiency of MB and the rate constants increased with increasing number of carboxyl groups in the presence of  $\alpha$ -OH because of the formation of  $\text{CO}_2^-$ . Upon the introduction of organic acids into the photo-Fenton system, the carboxyl groups of the organic acids would enhance the formation of  $\text{CO}_2^-$ , which can initiate MB degradation (Eq. (2)):



Moreover, the concentrations of dissolved  $\text{Fe}^{2+}$  and total Fe released from the composites have been reported to change when an organic acid is present in the solution (Fu et al., 2015; Yang et al., 2012). Therefore, in the present study, the role of the Fe species as well as that of noble metals during the catalytic process was evaluated. The concentrations of dissolved  $\text{Fe}^{2+}$  ion, total Fe, and  $\text{Ag}^+$  ion were measured in the presence of an organic acid in the Ag/Au/F-10G/ $\text{H}_2\text{O}_2$  system. The results are plotted in Figs. S2–S4. The results for Ag/Au/F-10G/ $\text{H}_2\text{O}_2$  in the absence of an organic acid and Ag/Au/F-10G in the absence of  $\text{H}_2\text{O}_2$  are also plotted. The concentrations of dissolved ions were less than the maximum permissible value established by the European Union (< 2 mg/L). The dissolved  $\text{Fe}^{2+}$ , total Fe, and  $\text{Ag}^+$  concentrations increased over time, reaching their maximum values at a reaction time of 45 min and then decreasing with further reaction time. In addition, the concentrations of dissolved ions in the presence of organic acids in the Ag/Au/F-10G system were less than those

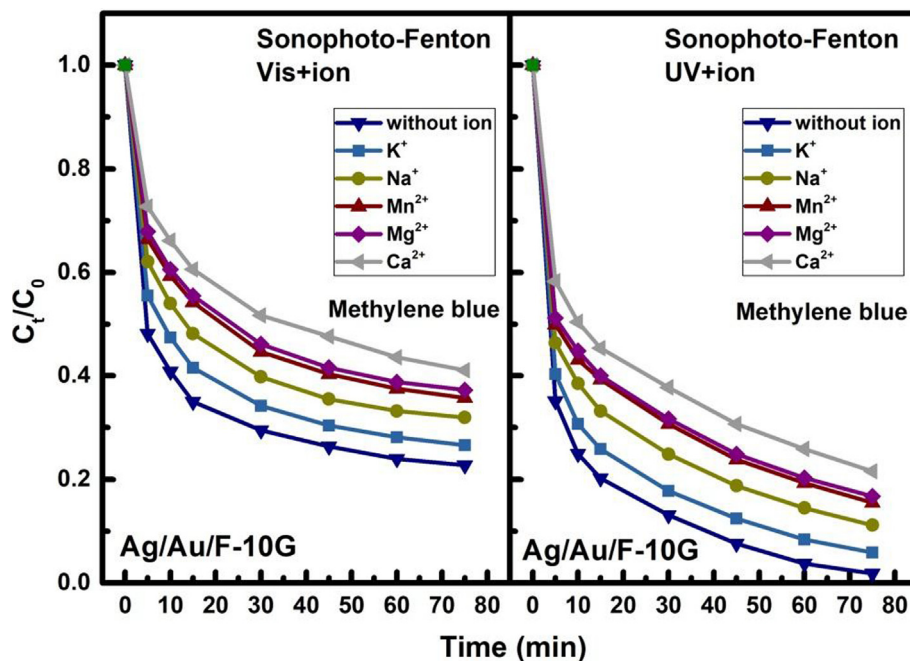


**Fig. 6** Influence of coexisting cations on the Fenton reactions of Ag/Au/F-10G composites under H<sub>2</sub>O<sub>2</sub> + MB + US irradiated with visible (left) and UV (right) light.

in the Ag/Au/F-10G/H<sub>2</sub>O<sub>2</sub> system without the addition of organic acids, suggesting that the dissolved Fe<sup>2+</sup>, total Fe, and Ag<sup>+</sup> ion concentrations were higher when only H<sub>2</sub>O<sub>2</sub> was added compared with their concentrations with the addition of an organic acid only. The concentrations of dissolved ions were even higher when an organic acid (i.e., AA) was added to the Ag/Au/F-10G/H<sub>2</sub>O<sub>2</sub> system. These results show that a correlation exists between the degradation efficiency and the ions dissolved in the solutions. Meanwhile, the evolution of temporal pH values during the reaction was characterized; the results are shown in Fig. S5. The pH values were found to be relatively unchanged during the catalytic processes.

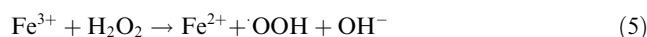
### 3.3. Influence of coexisting inorganic ions on catalytic performance of Ag/Au/F-10G

Contaminated industrial wastewaters usually contain not only synthetic dye waste but also substantial inorganic ions. The inorganic ions can either enhance or quench the removal efficiency or even influence the degradation of target pollutants. In a catalytic reaction involving H<sub>2</sub>O<sub>2</sub> and Fe species, the inorganic ions could lead to the formation of more or less Fe<sup>2+</sup> and Fe<sup>3+</sup> species and consequently affect the removal efficiency of the system. To understand the influence of inorganic ions on the removal of MB, we added various inorganic anions (I<sup>-</sup>, F<sup>-</sup>, SO<sub>4</sub><sup>2-</sup>, Cl<sup>-</sup>, H<sub>2</sub>PO<sub>4</sub><sup>-</sup>, NO<sub>3</sub><sup>-</sup>, and CO<sub>3</sub><sup>2-</sup>) and cations (K<sup>+</sup>, Na<sup>+</sup>, Mg<sup>2+</sup>, Mn<sup>2+</sup>, Ca<sup>2+</sup>) to an MB solution in the presence of H<sub>2</sub>O<sub>2</sub> and catalyst composites (Ag/Au/F-10G) under US + UV-light and US + visible-light irradiation. The concentration of the inorganic ions was chosen as 13 mM for both the anions and cations, and the initial pH value was adjusted to 5. Because the effect of Na<sup>+</sup> ions can

be neglected, the degradation of MB in the presence of coexisting SO<sub>4</sub><sup>2-</sup>, Cl<sup>-</sup>, H<sub>2</sub>PO<sub>4</sub><sup>-</sup>, NO<sub>3</sub><sup>-</sup>, CO<sub>3</sub><sup>2-</sup>, F<sup>-</sup>, and I<sup>-</sup> ions under US + UV-light and US + visible-light irradiation was evaluated; the results are plotted in Fig. 5. The anions negatively affected the degradation of MB. Specifically, the anions suppressed the degradation performance of MB in the sequence CO<sub>3</sub><sup>2-</sup> > NO<sub>3</sub><sup>-</sup> > Cl<sup>-</sup> > F<sup>-</sup> > H<sub>2</sub>PO<sub>4</sub><sup>-</sup> > SO<sub>4</sub><sup>2-</sup> > I<sup>-</sup>. The presence of CO<sub>3</sub><sup>2-</sup> strongly inhibited the degradation efficiency of MB. MB removal without the addition of CO<sub>3</sub><sup>2-</sup> was 77.24% and 98.17% under US + visible-light and US + UV-light irradiation, and it decreased by ~15% when CO<sub>3</sub><sup>2-</sup> was added. Similar to the removal of MB, the rate constant also decreased with the addition of CO<sub>3</sub><sup>2-</sup>. Carbonate ions are known to function as an effective scavenger for ·OH via the following reactions:



Notably, the oxidizing ability of CO<sub>3</sub><sup>2-</sup> is weaker than that of ·OH, resulting in the consumption of a large amount of ·OH (Wang et al., 2018). Moreover, the pH value substantially increased with increasing concentration of CO<sub>3</sub><sup>2-</sup>, indicating a buffering effect of CO<sub>3</sub><sup>2-</sup> ion. An increase of the pH of the solution and the scavenging effect of the ·OH quenching the regeneration of Fe<sup>2+</sup> ions are also evident in the reaction (Yu et al., 2016):



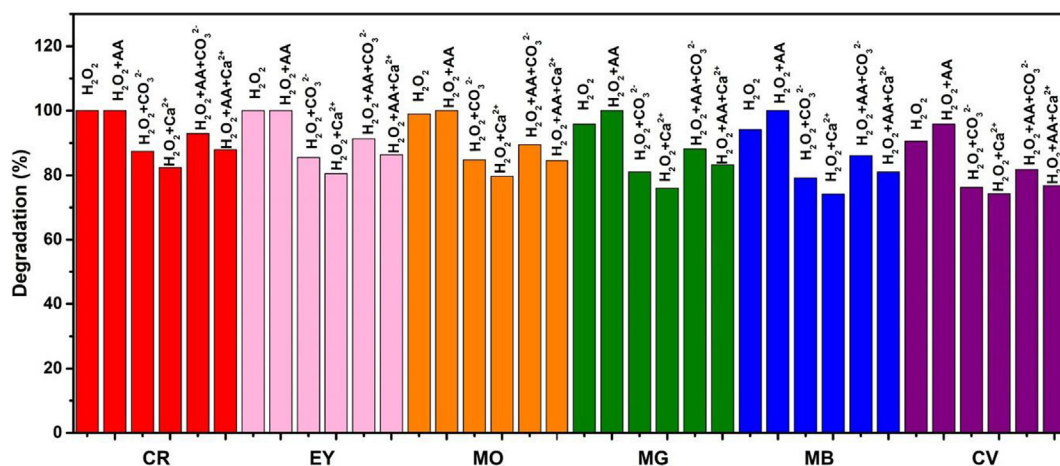


Fig. 7 Effect of CV, MG, CR, MO and EY on the Fenton reactions of Ag/Au/F-10G composites.

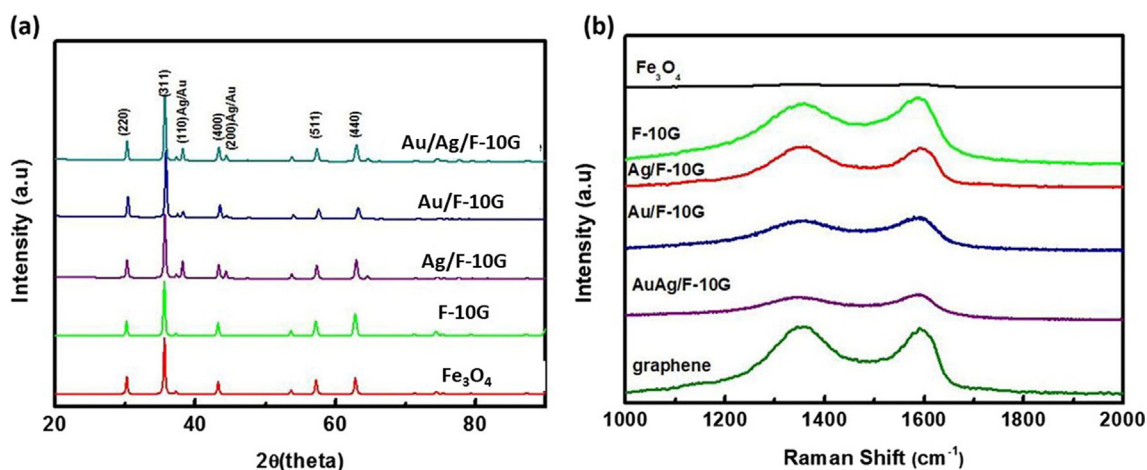


Fig. 8 (a) XRD patterns and (b) Raman spectra of the F, F-10G, Ag/F-10G, Au/F-10G, and Ag/Au/F-10G composite catalysts.

Fig. S6 shows the change in the leaching concentration of  $\text{Fe}^{2+}$  ions vs time during the degradation of MB. The leaching concentration of  $\text{Fe}^{2+}$  ions decreased because of the presence of  $\text{CO}_3^{2-}$  ions in the solutions.

Several researchers have found that the presence of a small amount of  $\text{NO}_3^-$  can enhance the photocatalytic efficiency because of the photolysis of  $\text{NO}_3^-$ . However, at higher concentrations such as those used in the present study, an inhibition of the degradation rate was observed when  $\text{NO}_3^-$  was added to the solution. Although the inhibition is not as high as in the case of  $\text{CO}_3^{2-}$ , the  $\text{NO}_3^-$  can act as a hole and  $\cdot\text{OH}$  scavenger. Moreover, competitive adsorption can occur when the solution contains excessive  $\text{NO}_3^-$  ions, leading to blocking of the catalyst surface and to a decrease of the reaction rate.

Numerous authors have reported that  $\text{Cl}^-$  ions have hole-scavenging properties. A  $\text{Cl}^-$  ion is oxidized by a hole to a  $\text{Cl}\cdot$  radical that is reduced back to a  $\text{Cl}^-$  ion by an electron. Thus, a  $\text{Cl}^-$  ion can either reduce a hole or scavenge an electron. Alternatively,  $\text{Cl}\cdot$  and  $\text{Cl}_2\cdot^-$  can further react with organic dye molecules via addition/elimination reactions (Tang et al., 2018; Wang et al., 2018). The influence of  $\text{Cl}^-$  ions can be described by the equations.



As reported in our previous study (Saleh and Taufik, 2019b), a  $\text{Cl}^-$  ion can undergo complex reactions with  $\text{Fe}^{2+}$  and  $\text{Fe}^{3+}$  ions, which hinders the reactions that produce  $\cdot\text{OH}$  radicals by preventing  $\text{Fe}^{2+}$  and  $\text{Fe}^{3+}$  complexes from catalyzing the decomposition of  $\text{H}_2\text{O}_2$ .

The influence of  $\text{F}^-$ ,  $\text{H}_2\text{PO}_4^-$ ,  $\text{SO}_4^{2-}$ , and  $\text{I}^-$  ions on the degradation of MB in the Ag/Au/F-10G/ $\text{H}_2\text{O}_2$  system under simultaneous US + light irradiation was also evaluated for various concentrations of ions. The presence of  $\text{F}^-$ ,  $\text{H}_2\text{PO}_4^-$ ,  $\text{SO}_4^{2-}$ , and  $\text{I}^-$  did not substantially affect the degradation of MB. The degradation of MB was inhibited by 75.38–67.81%, 76.39–69.32%, 76.39–70.57%, and 76.67–73.57% when  $\text{F}^-$ ,  $\text{H}_2\text{PO}_4^-$ ,  $\text{SO}_4^{2-}$ , and  $\text{I}^-$  were present under US + visible-light irradiation, respectively, as the concentration of the corresponding anions was increased from 2 to 26 mM (Fig. S7).

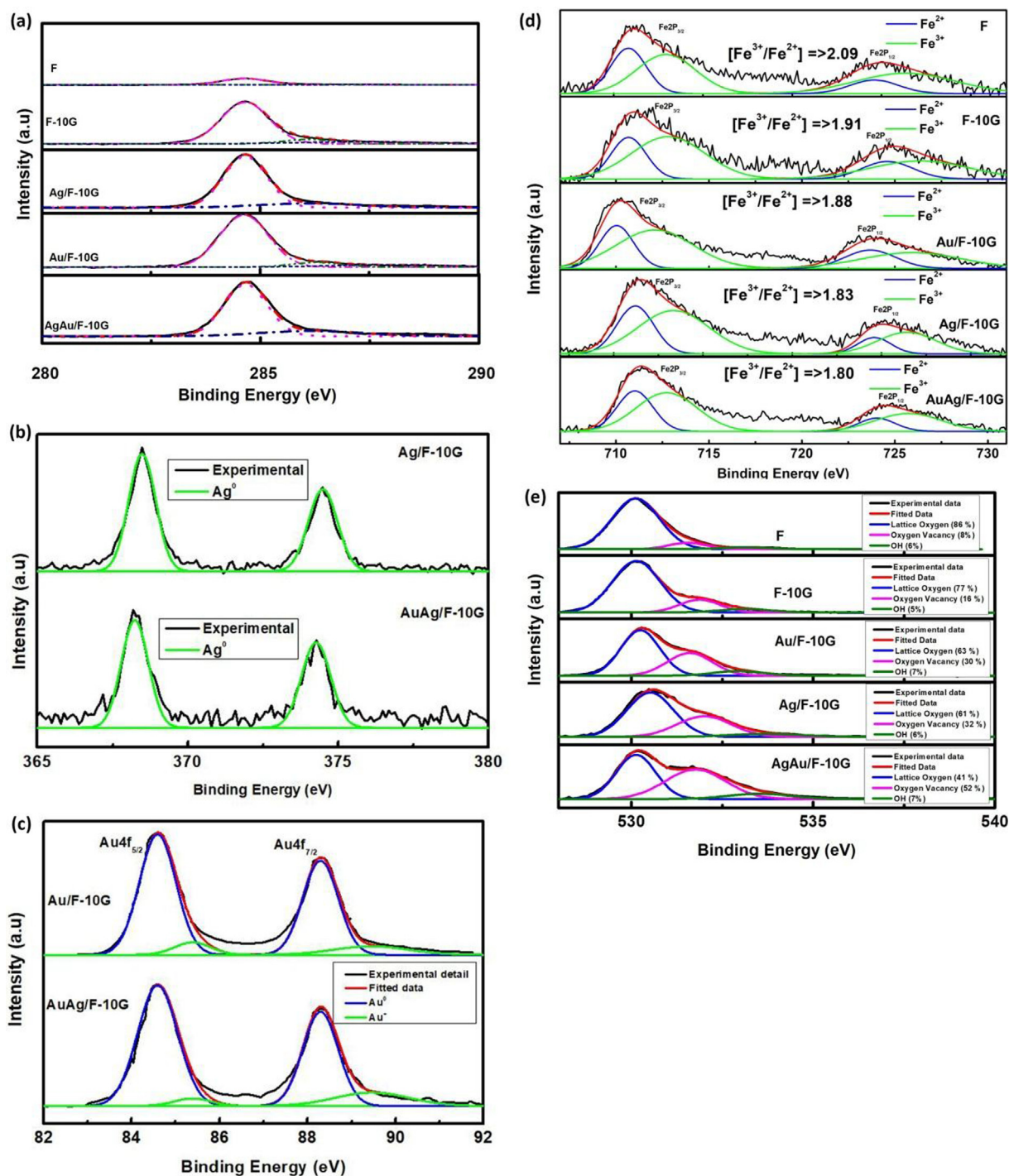


**Fig. 9** (a) C, (b) Ag, (c) Au, (d) Fe, and (e) O XPS spectra of the F, F-10G, Ag/F-10G, Au/F-10G, and Ag/Au/F-10G composite catalysts.

**Table 2** XPS peak area ratios of Au<sup>+</sup>/Au<sup>0</sup> and Ag<sup>+</sup>/Ag<sup>0</sup> in the Ag/F-10G, Au/F-10G, and Ag/Au/F-10G composite catalysts.

Sample	Ag <sup>+</sup>	Ag <sup>0</sup>	Ag <sup>0</sup> /Ag <sup>+</sup>	Au <sup>+</sup>	Au <sup>0</sup>	Au <sup>+</sup> /Au <sup>0</sup>
Ag/F-10G	0	1356				
Au/F-10G				3926	16,488	0.23
Ag/Au/F-10G	0	1324		2341	11,841	0.19

**Table 3** Grain size, specific surface area, pore size, pore volume, and magnetization of the F, F-10G, Ag/F-10G, Au/F-10G, and Ag/Au/F-10G composite catalysts.

Sample	Grain size (nm)			Surface Area (m <sup>2</sup> /g)	Average Pore Size (cm <sup>2</sup> /g)	Pore Volume (nm)	Magnetization (emu/g)
	Fe <sub>3</sub> O <sub>4</sub>	Au	Ag				
F	45	–	–	2.3	0.0377	11.27	81
F-10G	39	–	–	95	0.0865	14.75	89
Au/F-10G	38	22	–	56.45	0.0648	11.44	48
Ag/F-10G	38	–	22	81.45	0.0748	13.34	41
AgAu/F-10G	38	22	22	76.12	0.0656	12.34	21

The effect of cations (K<sup>+</sup>, Na<sup>+</sup>, Mg<sup>2+</sup>, Mn<sup>2+</sup>, Ca<sup>2+</sup>) on the degradation of MB under US + UV-light and US + visible-light irradiation is plotted in Fig. 6. Surprisingly, all five chloride salts exhibited an inhibition effect on the MB degradation process. Because these ions are in high and stable oxidation states and could not capture electrons or holes in the solution, we assumed that these ions would not substantially influence the degradation of MB. The inhibition effect could be related to the presence of Cl<sup>−</sup> ions in the solution. The greater inhibit effects of Ca<sup>2+</sup>, Mg<sup>2+</sup>, and Mn<sup>2+</sup> on the photodegradation of MB might be attributable to the Cl<sup>−</sup> concentration in the CaCl<sub>2</sub>, MgCl<sub>2</sub>, and MnCl<sub>2</sub> solutions being twice that in the KCl solution. (Tang et al., 2018).

### 3.4. Evaluation with other dyes

To further explore the Ag/Au/F-10G catalytic activity toward the removal of other dyes in the simultaneous presence of both an organic acid and inorganic ions, other cationic and anionic dyes such as CV, MG, CR, MO, and EY were investigated in the Ag/Au/F-10G/H<sub>2</sub>O<sub>2</sub> system under simultaneous US + UV-light irradiation. Operational parameters such as the initial dye concentration, catalyst loading, H<sub>2</sub>O<sub>2</sub> concentration, and pH were kept constant under the optimal conditions, and the same procedure used for the removal of MB was carried out. The results are depicted in Fig. 7. The Ag/Au/F-10G catalyst can potentially remove organic dyes in the Ag/Au/F-10G/H<sub>2</sub>O<sub>2</sub> system under UV + US irradiation. The degradation efficiency and the apparent rate constant followed the order CR (100% and 0.075 min<sup>−1</sup>) > EY (100%, 0.064 min<sup>−1</sup>) > MO (99.01%, 0.053 min<sup>−1</sup>) > MG (95.83%, 0.036 min<sup>−1</sup>) > MB (94.15%, 0.0326 min<sup>−1</sup>) > CV (90.54%, 0.027 min<sup>−1</sup>). The degradation efficiency of all of the dyes was accelerated upon the addition of AA; the reaction rate constants increased by 0.098, 0.075, 0.061, 0.052, 0.047, and 0.036 min<sup>−1</sup> for CR, EY, MO, MG, MG, and CV, respectively. Moreover, the coexistence of inorganic ions inhibited the degradation efficiency of all of the investigated dyes.

### 3.5. Characterization of catalyst

The X-ray diffraction (XRD) pattern of the synthesized Ag/Au/F-10G catalyst is shown in Fig. 8a. The XRD patterns of the F, F-10G, Ag/F-10G, and Au/F-10G catalysts are shown in the same figure. The diffraction peaks of Ag/Au/F-10G were indexed to a pure cubic spinel structure; intense peaks at 2θ values of 30.14°, 35.49°, 43.28°, 53.76°, 57.20°, and 62.83° correspond to the (2 2 0), (3 1 1), (4 0 0), (4 4 2),

(5 1 1), and (4 4 0) planes of the cubic spinel phase of Fe<sub>3</sub>O<sub>4</sub> in the Ag/Au/F-10G catalyst, respectively. As evident in Fig. 8a, the diffraction peaks at ~38.16° and ~44.37° correspond to the (1 1 0) and (2 0 0) planes of Au/Ag. Although the diffraction patterns of Ag and Au were relatively weak, Ag and Au were well incorporated into the Ag/Au/F-10G catalyst. No characteristic peaks of impurities or graphene were detected. The grain size of Fe<sub>3</sub>O<sub>4</sub>, Ag, and Au was calculated by using Bragg equation and the results were tabulated in Table 3. The grain size of each particle in the catalyst does not change significantly indicating that there is no structural change during composite formation.

To confirm the presence of graphene, Raman measurements were conducted. Fig. 8(b) shows the characteristic peaks of the G and D bands at 1605 and 1350 cm<sup>−1</sup>, which are typically assigned to the first-order scattering of the E<sub>2g</sub> mode and to the breathing mode of *k*-point phonons with A<sub>1g</sub> symmetry, respectively (El-Maghrabi et al., 2018; Wang et al., 2005). The intensity ratio between the D and G bands (*I*<sub>D</sub>/*I*<sub>G</sub>) is usually used to quantify the degree of disorder and the abundance of defects in graphitic materials. The intensity ratio (*I*<sub>D</sub>/*I*<sub>G</sub>) of 1.02 for the Ag/Au/F-10G catalyst is greater than that of pure graphene, indicating that the incorporation of Ag and Au induced structural disorder in the graphene.

The XPS spectrum of the Ag/Au/F-10G catalyst shows typical C 1s peaks of graphene (Fig. 9a). The peak at 284.65 eV is associated with sp<sup>2</sup> C and C–O, confirming the interaction between graphene and the Ag/Au/F-10G catalyst. The XPS survey spectrum shows peaks associated with Ag 3d, Au 4f, Fe 2p, and O 1s, confirming the presence of Ag, Au, Fe, O, and C elements in the Ag/Au/F-10G catalyst. Fig. 9b–e shows the high-resolution XPS spectra of Ag 3d, Au 4f, Fe 2p, and O 1s, respectively. The high-resolution XPS spectra of the F, F-10G, Ag/F-10G, and Au/F-10G catalysts are also shown. The two peaks at approximately 368.47 and 374.52 eV in Fig. 9b are attributed to the spin–orbit splitting of 3d<sub>5/2</sub> and 3d<sub>3/2</sub> of the Ag<sup>0</sup> electronic states. The relative area of each constituent peak decreased when Au was incorporated into the Ag/F-10G catalyst. Fig. 9c shows the two individual peaks located at 84.6 and 88.7 eV in the Au 4f spectrum, which are assigned to the spin–orbit splitting characteristic of 4f<sub>7/2</sub> and 4f<sub>5/2</sub>; the peaks can be further deconvoluted into peaks at binding energies of 84.6 and 88.7 eV corresponding to Au<sup>0</sup> and into other small peaks assigned to Au<sup>+</sup> at ~85.8 and ~89.7 eV. Notably, the Au<sup>+</sup>/Au<sup>0</sup> ratio (Table 2) also decreased when both noble metals (Ag and Au) were incorporated into the F-10G catalyst.

The Fe 2p XPS spectrum shown in Fig. 9e is split into Fe 2p<sub>3/2</sub> and Fe 2p<sub>1/2</sub> doublets at 710.69 eV and 724.36 eV because

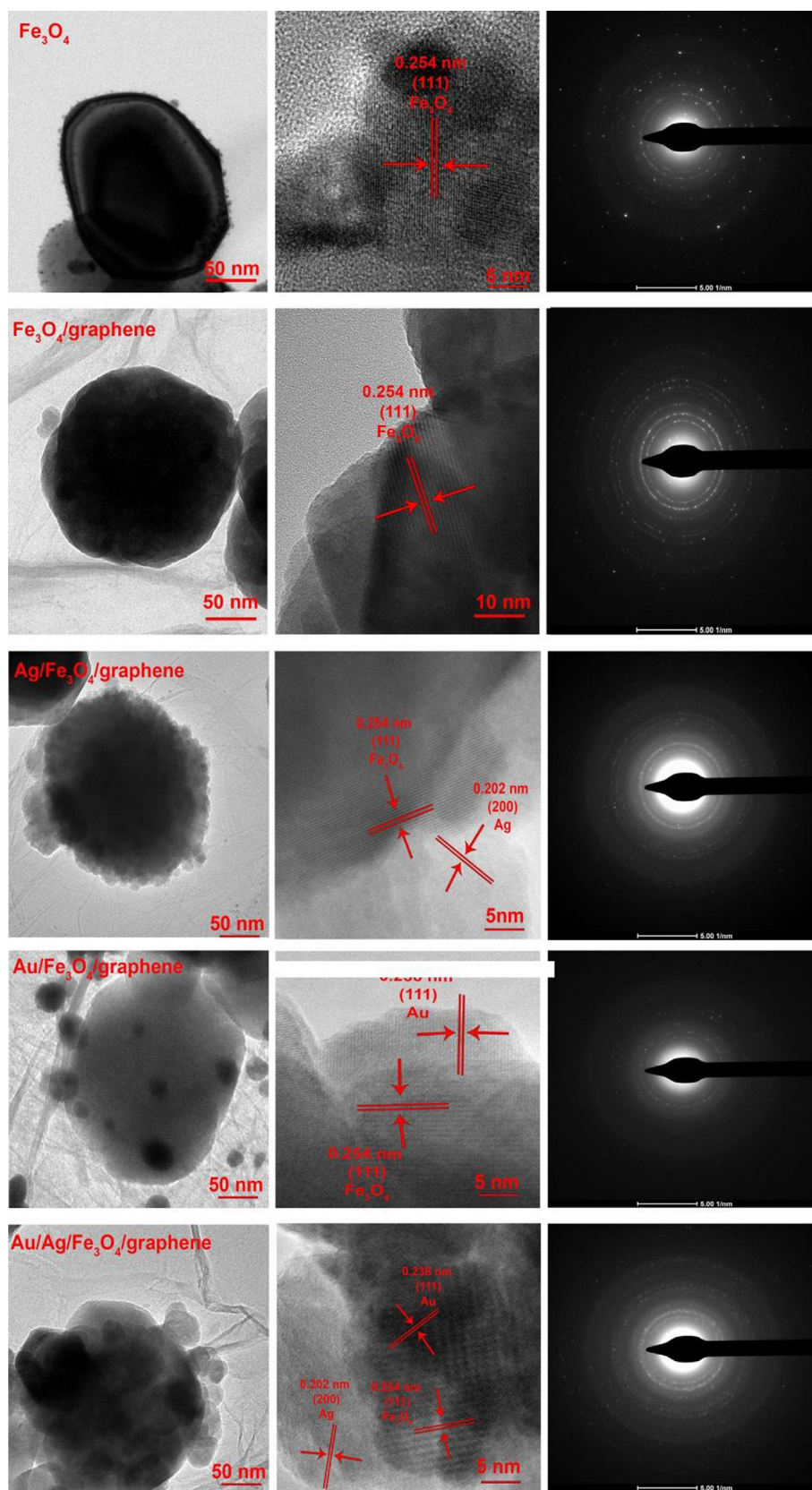


**Fig. 10** TEM and HRTEM images and SAED patterns of the F, F-10G, Ag/F-10G, Au/F-10G, and Ag/Au/F-10G composite catalysts.

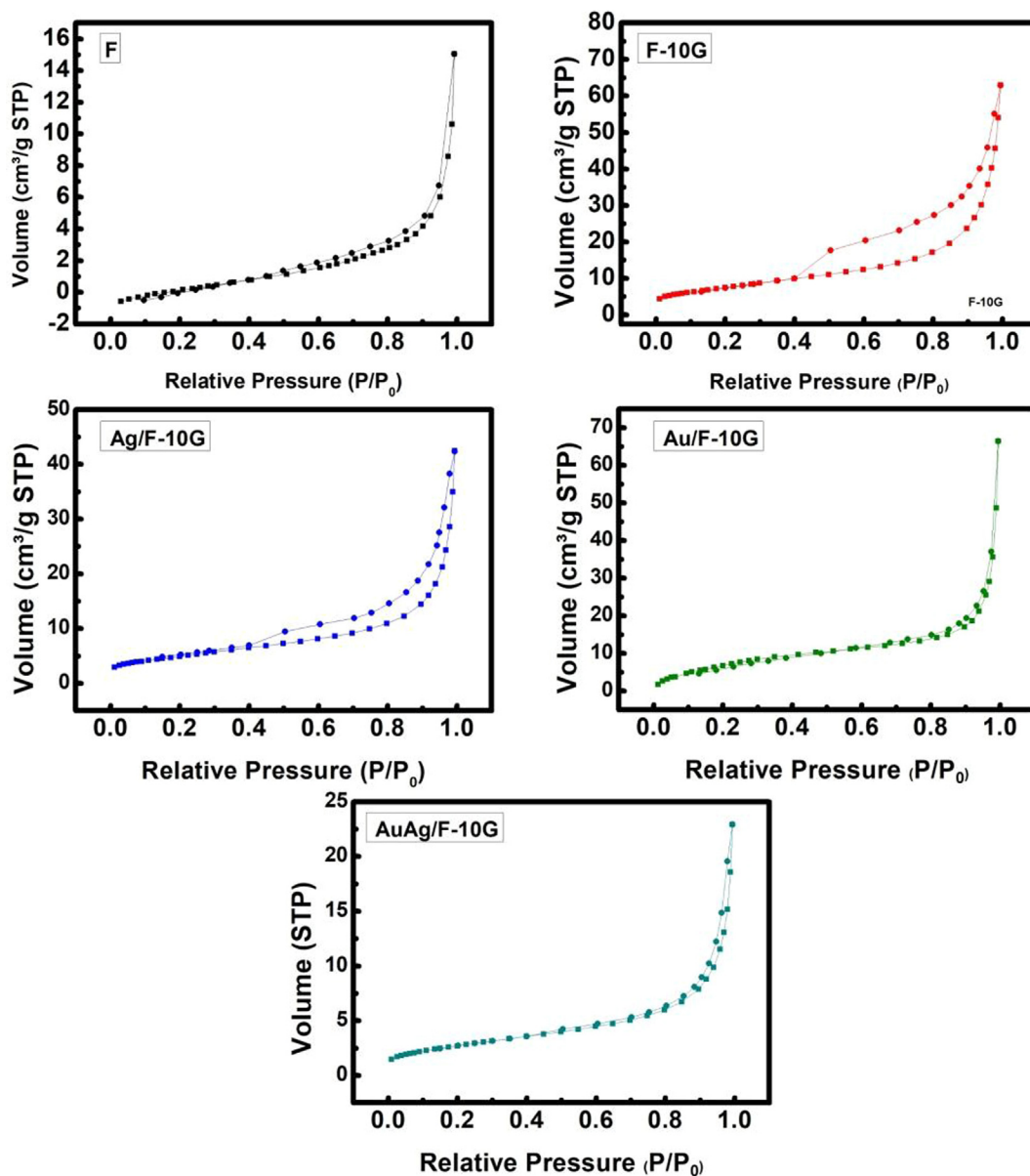


**Fig. 11**  $N_2$  adsorption–desorption isotherms of the F, F-10G, Ag/F-10G, Au/F-10G, Ag/Au/F-10G composites.

of spin–orbit coupling. Furthermore, both of these peaks can be deconvoluted into two peaks: one set at 710.26 and 724.10 eV, attributed to  $Fe^{3+}$ , and one set at 711.72 and 725.28 eV, assigned to  $Fe^{2+}$ . The mean relative areas of each constituent peak assigned to  $Fe^{3+}$  and  $Fe^{2+}$  (i.e., the  $Fe^{3+}/Fe^{2+}$  ratio) are also shown in the figure. Normally, in stoichiometric  $Fe_3O_4$ , the  $Fe^{3+}/Fe^{2+}$  ratio is 2:1. In the present study, the  $Fe^{3+}/Fe^{2+}$  ratio is 2.09, 1.91, 1.88, 1.83, and 1.80 for the F, F-10G, Ag/F-10G, and Au/F-10G catalysts, respectively, suggesting that the  $Fe^{3+}/Fe^{2+}$  ratio decreases with increasing incorporation of Au into F-10G and Ag/F-10G. These results show that some of the  $Fe^{3+}$  ions were reduced to  $Fe^{2+}$  ions when graphene was composited with the  $Fe_3O_4$  NPs and was reduced further when noble metals were coupled with the catalysts. Fig. 9e shows a broad peak of oxygen denoted by O 1s. This broad peak was deconvoluted into three separate peaks:

(i) a lattice oxygen peak with a binding energy of  $\sim 530.4$  eV, (ii) an oxygen vacancy peak at  $\sim 532.9$  eV, and (iii) a peak at  $\sim 533.56$  eV attributed to O–H at the surface of the composite particles. In the O 1s XPS spectra, the peak at a binding energy of 530.4 eV was enhanced when graphene was added to the F-10G catalyst. This peak was enhanced further when Ag and Au were incorporated into the F-10G catalyst and was amplified when both noble metals were coupled, indicating that a large number of oxygen vacancies were present in the catalyst. The ratio of Fe/Ag/Au were tabulated in Table S1. The ratio of Fe/Ag/Au were about 1:0.08:0.06.

The morphology of the synthesized Ag/Au/F-10G catalysts was studied by TEM, high-resolution TEM (HRTEM), and selected-area electron diffraction (SAED) measurements; the results are plotted in Fig. 10. Images of the F, F-10G, Ag/F-10G, and Au/F-10G catalysts are also plotted. Images of the

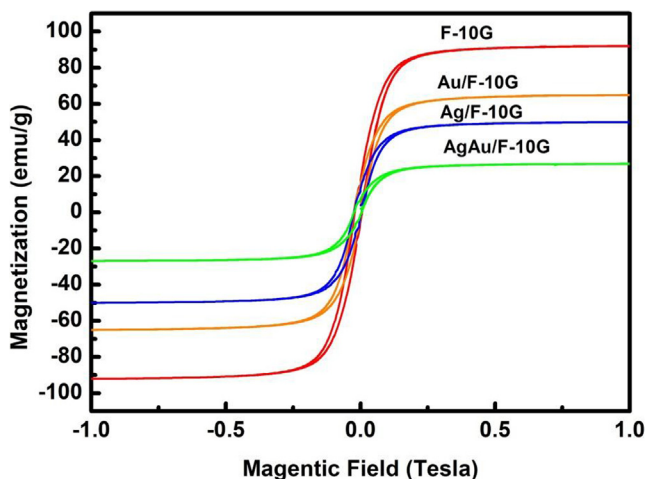


**Fig. 12** VSM magnetization curves of the F, F-10G, Ag/F-10G, Au/F-10G, and Ag/Au/F-10G composite catalysts.

Ag/Au/F-10G catalyst reveal lattice fringes with a  $d$ -spacing of 0.254 nm, which is attributed to the (1 1 1) plane of Fe<sub>3</sub>O<sub>4</sub>, a  $d$ -spacing of 0.238 nm corresponding to the (1 1 1) plane of Au, and a  $d$ -spacing of 0.202 nm. These results are consistent with the results of the XRD measurements. The SAED patterns indicate that all the samples exhibited high crystallinity.

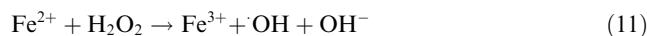
The specific surface area of the Ag/Au/F-10G catalysts were analyzed using the BET method from the results of N<sub>2</sub> adsorption–desorption measurements. Fig. 11 shows the N<sub>2</sub> adsorption–desorption isotherms of the Ag/Au/F-10G catalysts. The N<sub>2</sub> adsorption–desorption measurements of the F, F-10G, Ag/F-10G, and Au/F-10G catalysts are also shown. According to the International Union of Pure and Applied Chemistry (IUPAC) classification scheme, all of curves are identified as type IV with a H3 hysteresis loop, where a steep increase was observed in the high-pressure range. This result is attributable to the formation of pores between particles as a result of aggregation. The surface area and the pore size distribution of the corresponding sample are also tabulated in Table 3. The specific surface area of the Fe<sub>3</sub>O<sub>4</sub> NP catalyst

increased when graphene was composited with the Fe<sub>3</sub>O<sub>4</sub> NPs. However, with the addition of Ag, Ag + Au, and Au metals to the F-10G catalyst, the specific surface area of the catalyst decreased from 95 to 81.45, 76.12, and 56.45 m<sup>2</sup>/g, respectively.

In photocatalysis, magnetic materials are used because of their advantage of magnetic recyclability and reusability. Therefore, magnetization is an important parameter. The magnetization of the Ag/Au/F-10G catalyst is shown in Fig. 12. The magnetization curves for the F, F-10G, Ag/F-10G, and Au/F-10G catalysts are also plotted. The Ag/Au/F-10G catalyst still exhibited typical ferromagnetic hysteresis behavior although the saturation magnetization is lower than those of the Ag/F-10G and Au/F-10G catalysts. The corresponding saturation magnetization values are displayed in Table 3. As evident from Table 3, with the incorporation of noble metals, the saturation magnetization values decreased. The influence of graphene and the magnetization quenching effect due to the incorporation of noble metals have been discussed elsewhere (Taufik and Saleh, 2017b). Notably, the Ag/Au/F-10G catalyst is still strongly attracted by an external magnetic field and can still be completely separated from the solution within a short time.

### 3.6. Mechanism

On the basis of the experimental results, we propose the following reaction mechanism for the photosono-Fenton reaction involving Ag/Au/Fe<sub>3</sub>O<sub>4</sub>/graphene composites as illustrated in Fig. 13. The photosono-Fenton reaction of Au/Ag/Fe<sub>3</sub>O<sub>4</sub>/graphene an occur on the catalyst surface and also in the solution. The Fe<sup>2+</sup> and Fe<sup>3+</sup> ions are present both on the catalyst surface and in the solution because iron ions are leached from Fe<sub>3</sub>O<sub>4</sub>, react with H<sub>2</sub>O<sub>2</sub>, and produce ·OH (Yu et al., 2016):



Fe<sup>3+</sup> can also react with H<sub>2</sub>O<sub>2</sub> to produce Fe<sup>2+</sup>:

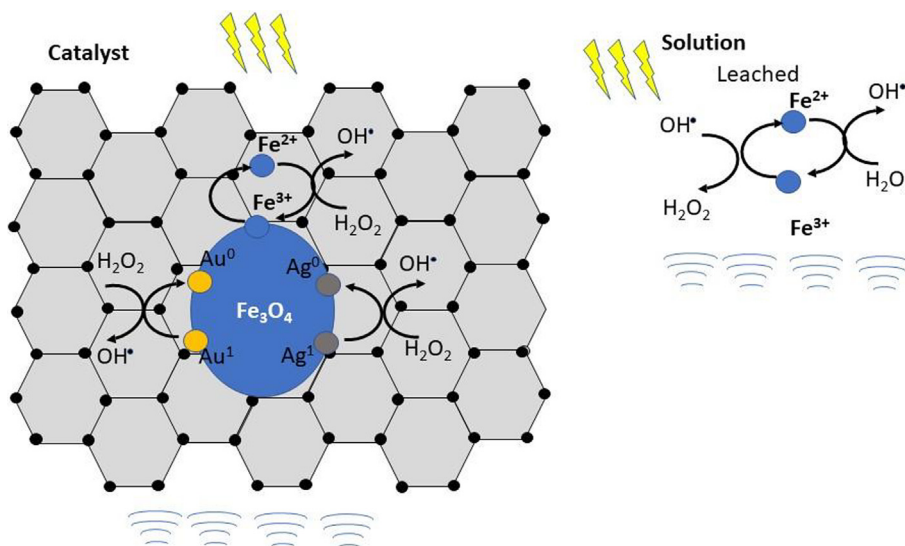
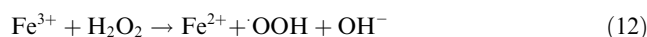


**Fig. 13** Proposed mechanism of dye degradation.

The reduction of  $\text{Fe}^{3+}$  to  $\text{Fe}^{2+}$  can also occur under UV- and visible-light irradiation:



Moreover, the inclusion of US irradiation, which enhances the concentration of  $\cdot\text{OH}$  radicals through a cavitation process, can further improve the degradation of organic pollutants:



The addition of graphene materials can improve the regeneration of  $\text{Fe}^{2+}$  because of the ability of graphene to transfer electrons via oxidation of  $\text{C}=\text{C}$ . Moreover, its high specific surface area promotes good dispersion of  $\text{Fe}_3\text{O}_4$  NPs into graphene sheets (Wang et al., 2017; Yang et al., 2012), enhancing the mass transfer of pollutants toward the active sites ( $\text{Fe}^{2+}/\text{Fe}^{3+}$ ) during the photo-Fenton reaction (Wang et al., 2017; Yaqoob et al., 2020a). The synergistic interaction between graphene and  $\text{Fe}_3\text{O}_4$  accelerates the  $\text{Fe}^{3+}/\text{Fe}^{2+}$  redox cycles and the efficient cyclical electron transfer between them is dominant in altering the surface redox processes. The Ag and Au also take a part on the degradation process because Ag and Au can release the electron and react with  $\text{O}_2$  to produce superoxide radicals and degrade the organic pollutant the double bond in  $\text{H}_2\text{O}_2$  can be activated by the  $\text{Ag}^0$  and  $\text{Au}^0$  generating  $\cdot\text{OH}$  and  $\text{Ag}^+$  as well as  $\text{Au}^+$ .



Moreover, in term of structural analysis, it could be seen that the specific surface area were gradually increase with the addition of Ag and Au altogether which can provide more active sites for the dye degradation. The oxygen vacancy also increase with the formation of Ag/Au/F-10G which became another active center for the degradation of methylene blue.

#### 4. Conclusion

Hydrothermally synthesized Ag/Au- $\text{Fe}_3\text{O}_4$ /graphene composites were applied for the degradation of MB in solution under simultaneous irradiation with light and US. The Ag and Au concentrations were fixed at 15 wt%, and the graphene content was fixed at 10 wt%. The physicochemical properties of the obtained catalysts were characterized using various methods, including X-ray diffraction, X-ray photoelectron spectroscopy, transmission electron microscopy,  $\text{N}_2$  adsorption/desorption isotherm measurements, UV-vis spectroscopy, and Raman spectroscopy. Catalysis experiments revealed that the removal efficiency of MB increased when Ag and Au were both incorporated in the  $\text{Fe}_3\text{O}_4$ /graphene/ $\text{H}_2\text{O}_2$  system compared to when Ag- $\text{Fe}_3\text{O}_4$ /graphene/ $\text{H}_2\text{O}_2$  and Au- $\text{Fe}_3\text{O}_4$ /graphene/ $\text{H}_2\text{O}_2$  systems were used, reflecting the important role of the synergistic interaction between the metallic NPs and the  $\text{Fe}_3\text{O}_4$ /graphene/ $\text{H}_2\text{O}_2$  systems. Moreover, the effect of the addition of organic acids and inorganic ions on the MB/ $\text{H}_2\text{O}_2$  system was investigated. Organic acid accelerated the degradation of the MB/ $\text{H}_2\text{O}_2$  system, whereas the addition of inorganic ions inhibited the degradation of MB in the Ag/Au- $\text{Fe}_3\text{O}_4$ /graphene/ $\text{H}_2\text{O}_2$  system.

#### Declaration of Competing Interest

The authors declare that they have no known competing financial interests or personal relationships that could have appeared to influence the work reported in this paper.

#### Acknowledgment

The author would like to thank Enago (www.enago.com) for the English language review. This work was financially supported in part by fund of grant Penelitian Universitas Indonesia under contract: NKB-1379/UN2.RST/HKP.05.00/2020.

#### Appendix A. Supplementary material

Supplementary data to this article can be found online at <https://doi.org/10.1016/j.arabjc.2022.103881>.

#### References

- Acharya, S., Mansingh, S., Parida, K.M., 2017. The enhanced photocatalytic activity of g- $\text{C}_3\text{N}_4$ - $\text{LaFeO}_3$  for the water reduction reaction through a mediator free Z-scheme mechanism. *Inorg. Chem. Front.* 4, 1022–1032. <https://doi.org/10.1039/c7qi00115k>.
- Ahmad, A., Mohd-Setapar, S.H., Chuong, C.S., Khatoon, A., Wani, W.A., Kumar, R., Rafatullah, M., 2015. Recent advances in new generation dye removal technologies: Novel search for approaches to reprocess wastewater. *RSC Adv.* <https://doi.org/10.1039/c4ra16959j>.
- Ahmad, H., Ahmad, A., Islam, S.S., 2017. Magnetic  $\text{Fe}_3\text{O}_4$ @poly(methacrylic acid) particles for selective preconcentration of trace arsenic species. *Microchim. Acta* 184, 2007–2014. <https://doi.org/10.1007/s00604-017-2214-3>.
- Amoli-Diva, M., Anvari, A., Sadighi-Bonabi, R., 2019. Synthesis of magneto-plasmonic Au-Ag NPs-decorated  $\text{TiO}_2$ -modified  $\text{Fe}_3\text{O}_4$  nanocomposite with enhanced laser/solar-driven photocatalytic activity for degradation of dye pollutant in textile wastewater. *Ceram. Int.* 45, 17837–17846. <https://doi.org/10.1016/j.ceramint.2019.05.355>.
- Barrera-Salgado, K.E., Ramírez-Robledo, G., Álvarez-Gallegos, A., Pineda-Arellano, C.A., Sierra-Espinosa, F.Z., Hernández-Pérez, J. A., Silva-Martínez, S., 2016. Fenton process coupled to ultrasound and UV light irradiation for the oxidation of a model pollutant. *J. Chem.* 2016. <https://doi.org/10.1155/2016/4262530>.
- Brinkmann, T., Hörsch, P., Sartorius, D., Frimmel, F.H., 2003. Photoformation of low-molecular-weight organic acids from brown water dissolved organic matter. *Environ. Sci. Technol.* 37, 4190–4198. <https://doi.org/10.1021/es0263339>.
- Costa, R.C.C., Lelis, M.F.F., Oliveira, L.C.A., Fabris, J.D., Ardisson, J.D., Rios, R.R.V.A., Silva, C.N., Lago, R.M., 2006. Novel active heterogeneous Fenton system based on  $\text{Fe}_3\text{-xMxO}_4$  (Fe Co, Mn, Ni): The role of  $\text{M}^{2+}$  species on the reactivity towards  $\text{H}_2\text{O}_2$  reactions. *J. Hazard. Mater.* 129, 171–178. <https://doi.org/10.1016/j.jhazmat.2005.08.028>.
- Cuerda-Correa, E.M., Alexandre-Franco, M.F., Fernández-González, C., 2020. Advanced oxidation processes for the removal of antibiotics from water. An overview. *Water (Switzerland)*. <https://doi.org/10.3390/w12010102>.
- Czibulya, Z., Horváth, I., Kollár, L., Nikfardjam, M.P., Kunsági-Máté, S., 2015. The effect of temperature, pH, and ionic strength on color stability of red wine. *Tetrahedron* 71, 3027–3031. <https://doi.org/10.1016/j.tet.2015.01.036>.
- Dükkancı, M., 2018. Sono-photo-Fenton oxidation of bisphenol-A over a  $\text{LaFeO}_3$  perovskite catalyst. *Ultrason. Sonochem.* 40, 110–116. <https://doi.org/10.1016/j.ultsonch.2017.04.040>.
- El-Maghrabi, H.H., Nada, A.A., Diab, K.R., Youssef, A.M., Hamdy, A., Roualdes, S., Abd El-Wahab, S., 2018. Facile fabrication of  $\text{NiTiO}_3$ /graphene nanocomposites for photocatalytic hydrogen generation. *J. Photochem. Photobiol. A* 365, 86–93. <https://doi.org/10.1016/j.jphotochem.2018.07.040>.
- Fu, Q., Zhou, X., Xu, L., Hu, B., 2015. Fulvic acid decorated  $\text{Fe}_3\text{O}_4$  magnetic nanocomposites for the highly efficient sequestration of

- Ni(II) from an aqueous solution. *J. Mol. Liq.* 208, 92–98. <https://doi.org/10.1016/j.molliq.2015.04.017>.
- Gu, S., Zhu, A., 2020. Graphene nanosheets loaded Fe<sub>3</sub>O<sub>4</sub> nanoparticles as a promising anode material for lithium ion batteries. *J. Alloy. Compd.* 813. <https://doi.org/10.1016/j.jallcom.2019.152160>.
- Jia, H., Chen, H., Nulaji, G., Li, X., Wang, C., 2015. Effect of low-molecular-weight organic acids on photo-degradation of phenanthrene catalyzed by Fe(III)-smectite under visible light. *Chemosphere* 138, 266–271. <https://doi.org/10.1016/j.chemosphere.2015.05.076>.
- Joseph, C.G., Li Puma, G., Bono, A., Krishnaiah, D., 2009. Sonophotocatalysis in advanced oxidation process: a short review. *Ultrason. Sonochem.* <https://doi.org/10.1016/j.ultsonch.2009.02.002>.
- Kumar, A., Kumaresan, T., Pandit, A.B., Joshi, J.B., 2006. Characterization of flow phenomena induced by ultrasonic horn. *Chem. Eng. Sci.*, 61, 7410–7420. <https://doi.org/10.1016/j.ces.2006.08.038>.
- Kumar, S.G., Rao, K.S.R.K., 2015. Zinc oxide based photocatalysis: Tailoring surface-bulk structure and related interfacial charge carrier dynamics for better environmental applications. *RSC Adv.* <https://doi.org/10.1039/c4ra13299h>.
- Liu, J., Zhao, Z., Ding, Z., Fang, Z., Cui, F., 2016. Degradation of 4-chlorophenol in a Fenton-like system using Au-Fe<sub>3</sub>O<sub>4</sub> magnetic nanocomposites as the heterogeneous catalyst at near neutral conditions. *RSC Adv.* 6, 53080–53088. <https://doi.org/10.1039/c6ra10929b>.
- López-Vinent, N., Cruz-Alcalde, A., Romero, L.E., Chávez, M.E., Marco, P., Giménez, J., Esplugas, S., 2019. Synergies, radiation and kinetics in photo-Fenton process with UVA-LEDs. *J. Hazard. Mater.* 380. <https://doi.org/10.1016/j.jhazmat.2019.120882>.
- Luciano, A.J.R., de Sousa Soletti, L., Ferreira, M.E.C., Cusioli, L.F., de Andrade, M.B., Bergamasco, R.N., Yamaguchi, N.U., 2020. Manganese ferrite dispersed over graphene sand composite for methylene blue photocatalytic degradation. *J. Environ. Chem. Eng.* 8. <https://doi.org/10.1016/j.jece.2020.104191>.
- Macías-Sánchez, J., Hinojosa-Reyes, L., Guzmán-Mar, J.L., Peralta-Hernández, J.M., Hernández-Ramírez, A., 2011. Performance of the photo-Fenton process in the degradation of a model azo dye mixture. *Photochem. Photobiol. Sci.* 10, 332–337. <https://doi.org/10.1039/c0pp00158a>.
- Magnus von Piechowski Marie-Anne Thelen, Jurg Hoign, and R.E.B., 1992. tert-Butanol as an OH-scavenger in the pulse radiolysis of oxygenated aqueous systems. *Ber. Bunsenges. Phys. Chem.* 96, 1448–1454.
- Mahalingam, S., Ahn, Y.H., 2018. Improved visible light photocatalytic activity of rGO-Fe<sub>3</sub>O<sub>4</sub>-NiO hybrid nanocomposites synthesized by: In situ facile method for industrial wastewater treatment applications. *New J. Chem.* 42, 4372–4383. <https://doi.org/10.1039/c8nj00013a>.
- Melgoza, D., Hernández-Ramírez, A., Peralta-Hernández, J.M., 2009. Comparative efficiencies of the decolourisation of Methylene Blue using Fenton's and photo-Fenton's reactions. *Photochem. Photobiol. Sci.* 8, 596–599. <https://doi.org/10.1039/b817287k>.
- Mishra, M., Chun, D.M., 2015.  $\alpha$ -Fe<sub>2</sub>O<sub>3</sub> as a photocatalytic material: A review. *Appl. Catal. A.* <https://doi.org/10.1016/j.apcata.2015.03.023>.
- Nguyen, X.S., Zhang, G., Yang, X., 2017. Mesocrystalline Zn-Doped Fe<sub>3</sub>O<sub>4</sub> Hollow Submicrospheres: Formation Mechanism and Enhanced Photo-Fenton Catalytic Performance. *ACS Appl. Mater. Interfaces* 9, 8900–8909. <https://doi.org/10.1021/acsami.6b16839>.
- Padhi, D.K., Panigrahi, T.K., Parida, K., Singh, S.K., Mishra, P.M., 2017. Green synthesis of Fe<sub>3</sub>O<sub>4</sub>/RGO nanocomposite with enhanced photocatalytic performance for Cr(VI) reduction, phenol degradation, and antibacterial activity. *ACS Sustainable Chem. Eng.* 5, 10551–10562. <https://doi.org/10.1021/acssuschemeng.7b02548>.
- Perreault, F., Fonseca De Faria, A., Elimelech, M., 2015. Environmental applications of graphene-based nanomaterials. *Chem. Soc. Rev.* 44, 5861–5896. <https://doi.org/10.1039/c5cs00021a>.
- Qian, X., Ren, M., Fang, M., Kan, M., Yue, D., Bian, Z., Li, H., Jia, J., Zhao, Y., 2018. Hydrophilic mesoporous carbon as iron(III)/(II) electron shuttle for visible light enhanced Fenton-like degradation of organic pollutants. *Appl. Catal. B* 231, 108–114. <https://doi.org/10.1016/j.apcatb.2018.03.016>.
- Saleh, R., Taufik, A., 2019a. Ultraviolet-light-assisted heterogeneous Fenton reaction of Ag-Fe<sub>3</sub>O<sub>4</sub>/graphene composites for the degradation of organic dyes. *J. Environ. Chem. Eng.* 7. <https://doi.org/10.1016/j.jece.2019.102895>.
- Saleh, R., Taufik, A., 2019b. Photo-Fenton degradation of methylene blue in the presence of Au-Fe<sub>3</sub>O<sub>4</sub>/graphene composites under UV and visible light at near neutral pH: Effect of coexisting inorganic anion. *Environ. Nanotechnol. Monit. Manage.* 11. <https://doi.org/10.1016/j.enmm.2019.100221>.
- Shokri, A., 2018. Application of Sono-photo-Fenton process for degradation of phenol derivatives in petrochemical wastewater using full factorial design of experiment. *Int. J. Indust. Chem.* 9, 295–303. <https://doi.org/10.1007/s40090-018-0159-y>.
- Singh, N., Prakash, J., Gupta, R.K., 2017. Design and engineering of high-performance photocatalytic systems based on metal oxide-graphene-noble metal nanocomposites. *Mol. Syst. Des. Eng.* <https://doi.org/10.1039/c7me00038c>.
- Sun, J., Mao, J.D., Gong, H., Lan, Y., 2009. Fe(III) photocatalytic reduction of Cr(VI) by low-molecular-weight organic acids with  $\alpha$ -OH. *J. Hazard. Mater.* 168, 1569–1574. <https://doi.org/10.1016/j.jhazmat.2009.03.049>.
- Sun, L., Chen, D., Wan, S., Yu, Z., Li, M., 2017. Role of small molecular weight organic acids with different chemical structures as electron donors in the photocatalytic degradation of ronidazole: synergistic performance and mechanism. *Chem. Eng. J.* 326, 1030–1039. <https://doi.org/10.1016/j.cej.2017.06.053>.
- Tang, T., Lu, G., Wang, W., Wang, R., Huang, K., Qiu, Z., Tao, X., Dang, Z., 2018. Photocatalytic removal of organic phosphate esters by TiO<sub>2</sub>: effect of inorganic ions and humic acid. *Chemosphere* 206, 26–32. <https://doi.org/10.1016/j.chemosphere.2018.04.161>.
- Taufik, A., Saleh, R., 2017a. Organic dyes removal using magnetic Fe<sub>3</sub>O<sub>4</sub>-nanographene platelets composite materials. *Physica B* 526, 166–171. <https://doi.org/10.1016/j.physb.2016.09.014>.
- Taufik, A., Saleh, R., 2017b. Synergistic effect between ternary iron-zinc-copper mixed oxides and graphene for photocatalytic water decontamination. *Ceram. Int.* 43, 3510–3520. <https://doi.org/10.1016/j.ceramint.2016.10.176>.
- Vinothkannan, M., Karthikeyan, C., Gnana Kumar, G., Kim, A.R., Yoo, D.J., 2015. One-pot green synthesis of reduced graphene oxide (RGO)/Fe<sub>3</sub>O<sub>4</sub> nanocomposites and its catalytic activity toward methylene blue dye degradation. *Spectrochim. Acta – Part A: Mol. Biomol. Spectrosc.* 136, 256–264. <https://doi.org/10.1016/j.saa.2014.09.031>.
- Wan, Z., Wang, J., 2017. Fenton-like degradation of sulfamethazine using Fe<sub>3</sub>O<sub>4</sub>/Mn<sub>3</sub>O<sub>4</sub> nanocomposite catalyst: kinetics and catalytic mechanism. *Environ. Sci. Pollut. Res.* 24, 568–577. <https://doi.org/10.1007/s11356-016-7768-9>.
- Wang, H., You, C., Tan, Z., 2018. Enhanced photocatalytic oxidation of SO<sub>2</sub> on TiO<sub>2</sub> surface by Na<sub>2</sub>CO<sub>3</sub> modification. *Chem. Eng. J.* 350, 89–99. <https://doi.org/10.1016/j.cej.2018.05.128>.
- Wang, J., Guo, B., Zhang, X., Zhang, Z., Han, J., Wu, J., 2005. Sonocatalytic degradation of methyl orange in the presence of TiO<sub>2</sub> catalysts and catalytic activity comparison of rutile and anatase. *Ultrason. Sonochem.* 12, 331–337. <https://doi.org/10.1016/j.ultsonch.2004.05.002>.
- Wang, L., Xie, L., Zhao, W., Liu, S., Zhao, Q., 2021. Oxygen-facilitated dynamic active-site generation on strained MoS<sub>2</sub> during photo-catalytic hydrogen evolution. *Chem. Eng. J.* 405. <https://doi.org/10.1016/j.cej.2020.127028>.
- Wang, P., Huang, B., Dai, Y., Whangbo, M.H., 2012. Plasmonic photocatalysts: Harvesting visible light with noble metal nanoparticles. *PCCP.* <https://doi.org/10.1039/c2cp40823f>.

- Wang, P., Zhou, X., Zhang, Y., Yang, L., Zhi, K., Wang, L., Zhang, L., Guo, X., 2017. Unveiling the mechanism of electron transfer facilitated regeneration of active  $\text{Fe}^{2+}$  by nano-dispersed iron/graphene catalyst for phenol removal. *RSC Adv.* 7, 26983–26991. <https://doi.org/10.1039/c7ra04312k>.
- Xuan, S., Wang, F., Lai, J.M.Y., Sham, K.W.Y., Wang, Y.X.J., Lee, S.F., Yu, J.C., Cheng, C.H.K., Leung, K.C.F., 2011. Synthesis of biocompatible, mesoporous  $\text{Fe}_3\text{O}_4$  nano/microspheres with large surface area for magnetic resonance imaging and therapeutic applications. *ACS Appl. Mater. Interfaces* 3, 237–244. <https://doi.org/10.1021/am1012358>.
- Yang, F., Feng, A., Wang, C., Dong, S., Chi, C., Jia, X., Zhang, L., Li, Y., 2016. Graphene oxide/carbon nanotubes- $\text{Fe}_3\text{O}_4$  supported Pd nanoparticles for hydrogenation of nitroarenes and C-H activation. *RSC Adv.* 6, 16911–16916. <https://doi.org/10.1039/c5ra25842a>.
- Yang, S., Zong, P., Ren, X., Wang, Q., Wang, X., 2012. Rapid and highly efficient preconcentration of Eu(III) by core-shell structured  $\text{Fe}_3\text{O}_4$ @Humic acid magnetic nanoparticles. *ACS Appl. Mater. Interfaces* 4, 6891–6900. <https://doi.org/10.1021/am3020372>.
- Yaqoob, A.A., Ahmad, H., Parveen, T., Ahmad, A., Oves, M., Ismail, I.M.I., Qari, H.A., Umar, K., Mohamad Ibrahim, M.N., 2020a. Recent advances in metal decorated nanomaterials and their various biological applications: a review. *Front. Chem.* <https://doi.org/10.3389/fchem.2020.00341>.
- Yaqoob, A.A., Parveen, T., Umar, K., Ibrahim, M.N.M., 2020b. Role of nanomaterials in the treatment of wastewater: a review. *Water* (Switzerland). <https://doi.org/10.3390/w12020495>.
- Yaqoob, A.A., Umar, K., Ibrahim, M.N.M., 2020c. Silver nanoparticles: various methods of synthesis, size affecting factors and their potential applications—a review. *Appl. Nanosci.* (Switzerland). <https://doi.org/10.1007/s13204-020-01318-w>.
- Yaqoob, A.A., Rameez Khan, M., Saddique, A., Pakistan, K., n.d. Review article on applications and classification of gold nanoparticles. *Int. J. Res.* Available.
- Yehia, F.Z., Badawi, A.M., Eshaq, G., Dimitry, O.I.H., 2015. Investigation on the sonocatalytic degradation of nitrobenzene using heterogeneous nanostructured catalysts in absence and presence of surfactant. *Egypt. J. Pet.* 24, 265–276. <https://doi.org/10.1016/j.ejpe.2015.07.011>.
- Yu, L., Chen, J., Liang, Z., Xu, W., Chen, L., Ye, D., 2016. Degradation of phenol using  $\text{Fe}_3\text{O}_4$ -GO nanocomposite as a heterogeneous photo-Fenton catalyst. *Sep. Purif. Technol.* 171, 80–87. <https://doi.org/10.1016/j.seppur.2016.07.020>.
- Zhang, L.i., Wu, Z., Chen, L., Zhang, L., Li, X., Xu, H., Wang, H., Zhu, G., 2016. Preparation of magnetic  $\text{Fe}_3\text{O}_4/\text{TiO}_2/\text{Ag}$  composite microspheres with enhanced photocatalytic activity. *Solid State Sci.* 52, 42–48. <https://doi.org/10.1016/j.solidstatesciences.2015.12.006>.
- Zhu, L., Kong, X., Yang, C., Ren, B., Tang, Q., 2020. Fabrication and characterization of the magnetic separation photocatalyst  $\text{C-TiO}_2@ \text{Fe}_3\text{O}_4/\text{AC}$  with enhanced photocatalytic performance under visible light irradiation. *J. Hazard. Mater.* 381. <https://doi.org/10.1016/j.jhazmat.2019.120910>.